

1 **Mechanical Stratigraphy Controls Normal Fault Growth and Dimensions, Outer**  
2 **Kwanza Basin, Offshore Angola**

3  
4 **David Redpath<sup>1\*</sup>, Christopher A.-L Jackson<sup>1</sup>, Rebecca E. Bell<sup>1</sup>**

5 Basins Research Group (BRG), Department of Earth Science & Engineering, Imperial  
6 College, Prince Consort Road, London, SW7 2BP, UK

7 \*Corresponding author: David Redpath ([david.redpath16@imperial.ac.uk](mailto:david.redpath16@imperial.ac.uk))

8 *This paper is a non-peer reviewed preprint submitted to EarthArXiv. This preprint has been*  
9 *submitted to AGU Tectonics for consideration for publication.*

10

11

12 **Key Points:**

- 13 • Mechanical stratigraphy and fault interaction control the extent to which faults adhere  
14 to displacement-length scaling relationships.
- 15 • Fault growth and displacement-length relationships must be considered in context of  
16 local controls to be adequately described.
- 17 • Detailed kinematic analysis on faults developing within the same overall tectono-  
18 stratigraphic setting can shed light on the kinematics of blind fault growth.

19

20

21

## 22 **Abstract**

23 Fault growth and dimensions are controlled by mechanical stratigraphy on seismic scales. Here  
24 we present a detailed analysis of largely blind faults and their kinematics Offshore, Angola;  
25 where, salt bodies and mass-transport complexes (MTC) act as mechanically restricting  
26 elements to an array of extensional faults. Our study presents mechanically restricted faults  
27 whose data fall within the general scatter present in global displacement-length (D-L) scaling  
28 datasets, and yet have starkly different fault growth models to those expected using geometric  
29 data alone. We show how using displacement-length data to determine fault growth can mask  
30 the not insignificant mechanical controls on growth histories in the absence of detailed  
31 kinematic analysis. We present how fault growth and displacement-length scaling relationships  
32 must be considered within the context of local mechanical stratigraphy, stress-fields and fault  
33 interaction and that conducting such studies across varying scales can provide more robust  
34 kinematic constraints in adequately determining displacement-length relationships and fault  
35 growth.

36 **Key Words:** Fault growth; Fault scaling; Fault geometry, Mechanical stratigraphy; Fault  
37 kinematics

## 38 **1.0 Introduction**

39 Understanding the geometry and growth of normal faults is crucial for a range of geoscience  
40 disciplines. For example, these structures control landscape evolution and sediment transport  
41 pathways in areas of continental extension (e.g. Gibbs, 1984, Leeder and Gawthorpe, 1987,  
42 McClay, 1990, Gawthorpe and Hurst, 1993, Trudgill and Cartwright, 1994, Peacock and  
43 Sanderson, 1994, Eliet and Gawthorpe, 1995, Gawthorpe and Leeder, 2000, Childs et al.,  
44 2003), the magnitude and recurrence interval of potentially hazardous earthquakes (e.g. Cowie  
45 and Scholz, 1992b, Walsh et al., 2002, Soliva et al., 2008, Wilkinson et al., 2015), and the

46 occurrence and viability of hydrocarbon and geothermal resources (e.g. Bodvarsson et al.,  
47 1982, Fairley and Hinds, 2004, Rotevatn et al., 2007, Athmer and Luthi, 2011, Corbel et al.,  
48 2012, Serié et al., 2017).

49 Fault growth models were originally derived from global compilations of displacement (D) and  
50 length (L) data. More specifically, the recognition that D and L were positively correlated over  
51 several-orders-of-magnitude in the form  $D = cL^n$  led to the development of the so-called  
52 ‘propagating’ fault model, in which faults grow via a sympathetic increase in their  
53 displacement and length (e.g. Walsh and Watterson, 1988, Cartwright et al., 1995, Walsh et  
54 al., 2003, Nicol et al., 2005, Rotevatn et al., 2018, Nicol et al., 2020). More recent observations,  
55 primarily from 3D seismic reflection data, have supported an alternative model for normal fault  
56 growth; in this, the so-called ‘constant-length’ fault model, faults rapidly establish their near-  
57 final length before accumulating significant displacement (e.g. Walsh et al., 2002, Rotevatn et  
58 al., 2018). Rotevatn et al. (2018) also propose a hybrid growth model in which rapid fault  
59 lengthening by tip propagation, and ultimately segment linkage – characteristics most  
60 consistent with the propagating fault model - occurs for the initial 20-30% of the fault lifespan  
61 (stage 1). This is followed by a second, more prolonged period of displacement accrual, during  
62 which time the fault does not significantly lengthen – characteristics more representative of the  
63 constant-length model (stage 2).

64 The lithological and rheological heterogeneity of the host rock can influence the nucleation,  
65 growth, and ultimate geometry of faults. More specifically, the vertical and lateral propagation  
66 of faults that nucleate in competent layers (e.g. brittle carbonate) can be impeded vertically and  
67 laterally as they approach, deform, and mechanically interact with less competent layers (e.g.  
68 ductile salt or mudstone), a situation common in heterogeneous sedimentary sequences. This  
69 behaviour can result in anomalous fault aspect ratios (i.e. the ratio between maximum fault  
70 height and length) and a deviation from the expected D-L relationship (Wilkins and Gross,

71 2002, Soliva et al., 2005a, Soliva and Benedicto, 2005). For example, a fault may preferentially  
72 propagate along-strike (i.e. laterally) in competent layers, thereby restricting its vertical height  
73 and increasing its aspect ratio, as well as restricting its ability to accumulate displacement and  
74 thus causing them to appear ‘under-displaced’. Short- and long-range stress interactions  
75 between salt bodies and faults (e.g. Tvedt et al., 2013), and between neighbouring faults (e.g.  
76 Peacock and Sanderson, 1991, Dawers and Anders, 1995, Martel, 1999, Peacock, 2002, Soliva  
77 et al., 2006), can also influence fault growth and geometry.

78 In this study, we use high-quality 3D seismic reflection data acquired by CGG from the Outer  
79 Kwanza Basin, offshore Angola to quantify the geometry of and displacement patterns on  
80 several normal faults (Fig. 1 and 2). These data allow us to assess how host rock mechanical  
81 properties, inferred from seismic facies analysis, influence fault growth and ultimate  
82 geometry, thereby allowing us to test fault growth models. These faults occur in a host rock  
83 dominated by slope mudstones, within which mechanical layering is imposed by a regionally  
84 developed mass-transport complex (MTC). The faults formed in a broadly similar stress  
85 regime, and therefore that any differences in their geometry and kinematics likely reflect the  
86 host rock heterogeneity and local mechanical interactions. We show that the aspect ratios and  
87 displacement patterns vary on even closely spaced faults. We explore why faults can deviate  
88 from D-L scaling laws as they grow, even when they presently have D-L scaling relationships  
89 that broadly adhere to global compilations ( $D = cL^n$ ; Fig. 2). Our study shows that D-L  
90 scaling (i.e. geometric) data alone does not allow us to determine the style of fault growth;  
91 detailed kinematic analysis using growth strata (e.g. Tvedt et al., 2013, Duffy et al., 2015),  
92 and the analysis of faults of varying scales within a single population, together provide more  
93 robust kinematic constraints.

94

## 95 **2 Data and Methods**

96 *2.1 Data*

97 The study area is imaged by a high-quality, pre-stack, depth-migrated (PDSM) BroadSeis™  
98 3D survey with an aerial extent of 2915 km<sup>2</sup> (Fig. 1). The inline and crossline spacing for the  
99 survey is 25 m, with a vertical sampling interval of 2 m. The data are normal polarity (a peak  
100 indicates a downward increase in acoustic impedance) and zero phase, with a vertical resolution  
101 of c. 6 m at the seabed and c. 30 m at a depth of 3.5 km, approximated by a quarter of the  
102 dominant wavelength of the data (assuming average P-wave velocity of 2500 m/s). In the  
103 absence of well-data, the lithology and absolute ages of the mapped seismic-stratigraphic units  
104 are constrained by using seismic facies analysis, seismic-stratigraphic principles, and by  
105 correlating their bounding horizons with three regionally mapped horizons (the Top Albian,  
106 Top Eocene and Top Miocene) presented by Hudec and Jackson (2004) (See also  
107 Spathopoulos, 1996, Marton et al., 2000, Hudec and Jackson, 2003, Hudec and Jackson, 2004,  
108 Jackson et al., 2005, Jackson and Hudec, 2008, Serié et al., 2017). The ages of other mapped  
109 horizons are inferred relative to these regional surfaces and documented geological events (e.g.  
110 periods of continental uplift and related salt tectonics). We use these age estimates to infer at  
111 which stratigraphic levels fault throw maxima occur, which may relate to the depth at which  
112 the faults nucleated (e.g. Hongxing and Anderson, 2007).

113 *2.2 Seismic interpretation and fault characterisation*

114 We study a c. 70 km<sup>2</sup> area that is located between a c. 10 km long salt wall and a salt stock, the  
115 latter of which is only partially imaged along the western edge of the seismic survey (Fig. 1  
116 and 3). Within this area we focus on sixteen, exceptionally well-imaged normal faults that form  
117 part of a larger array (Fig. 4 and 5). These faults are also selected because we can  
118 comprehensively map numerous (18) horizons in their flanking host rocks and, therefore,  
119 generate 3D throw strike-projections that allow us to constrain throw distributions across their

120 surfaces (e.g. Walsh et al., 2003, Baudon and Cartwright, 2008, Duffy et al., 2015). We  
121 accurately mapped the faults on closely spaced (*c.* 50 m) seismic sections trending normal to  
122 fault strike. We therefore constrain their three-dimensional geometry, including their aspect  
123 ratio (i.e. length/down-dip height), with reasonable precision (Fig. 6) (Nicol et al., 1996, Polit  
124 et al., 2009). Where fault-related folding of the host rock is present adjacent to the fault  
125 surfaces, the cutoffs are extrapolated to remove the effects of this ductile or continuous  
126 deformation (e.g. Walsh and Watterson, 1987, Hongxing and Anderson, 2007, Jackson et al.,  
127 2017).

128 Shallow stratigraphy (*c.* 0-300 m below seabed) in the study area contains deep-water channels  
129 that incise up to 200 m into underlying stratigraphy (Fig. 7). This makes it difficult to  
130 confidently and regionally map near-seabed growth sequences that are now eroded (i.e. F6 and  
131 7) (Fig. 7). Since many of the faults in the study area have shallow upper tips, where extensive  
132 channel-driven erosion occurs at the top of the fault (i.e. F3) it may be the case that aspect  
133 ratios become slightly higher than the original fault geometry (Fig. 6).

134 We follow the method of Walsh and Watterson (1991) to construct throw-distance (T-x) plots  
135 that show how throw varies along-strike on a given horizon, as well as strike-projections that  
136 show the throw distribution across the fault surface (e.g. Fig. 8) (Tvedt et al., 2013, Duffy et  
137 al., 2015, Collanega et al., 2018, Torabi et al., 2019). We also calculate throw gradients (i.e.  
138 change in throw/distance on fault surface over which the change occurs) across the fault  
139 surface, noting that relatively high gradients ( $> 0.15$ ) may reflect retardation of fault tip  
140 propagation due to mechanical interactions with adjacent faults or host rock layers (e.g. Walsh  
141 and Watterson, 1988, Nicol et al., 1996). To determine where faults intersected the free surface  
142 during their growth, we calculate the expansion indices (EI) of packages of growth strata; EI  
143 is calculated by dividing the hanging-wall thickness of the package by its adjacent footwall  
144 thickness (e.g. Tvedt et al., 2013, Jackson et al., 2017). Finally, we define down-dip fault height

145 (H) as the (sub)vertical distance from the fault upper to lower tip, and fault length (L) as the  
146 maximum (sub)horizontal distance between the faults lateral tips (Fig. 6). Using these  
147 geometric data we determine fault aspect ratio (fault length/down-dip height of fault), which  
148 again can be used to infer whether the growth of a fault has been inhibited by mechanical  
149 interactions with adjacent faults or changes in host rock mechanical properties (Nicol et al.,  
150 1996, Soliva et al., 2005b).

### 151 **3 Geological Setting**

#### 152 *3.1 Outer Kwanza Basin*

153 The Angolan continental margin comprises a series of basins formed during the break-up of  
154 Gondwana (Brice et al., 1982, Serié et al., 2017). The formation of the Inner and Outer Kwanza  
155 basins, offshore Angola initiated in the Early Cretaceous when rift pulses between the African  
156 and South American plates ultimately resulted in the opening of the South Atlantic Ocean  
157 (Brice et al., 1982, Jackson et al., 2005, Hudec and Jackson, 2004) (Fig. 1).

158 During the Early Cretaceous, intermittent marine incursions resulted in restricted marine  
159 conditions and the deposition of thick, Aptian-Albian evaporites in the Inner and Outer Kwanza  
160 basins (e.g. Bate et al., 2001, Karner and Gambôa, 2007). Flow of this evaporite sequence from  
161 the Late Cretaceous until present controlled the overall, post-breakup structural evolution of  
162 the Kwanza Basins (Marton et al., 2000, Hudec and Jackson, 2004, Jackson and Hudec, 2008).  
163 For example, basinward tilting of the margin during the Late Cretaceous initiated the first post-  
164 salt phase of extension, causing the formation of predominantly seaward-dipping, salt-detached  
165 normal faults (Jackson et al., 2005). Post-salt deposition was initially dominated by relatively  
166 fine-grained deep-water sediments of the Iabe Group (Hudec and Jackson, 2003, Hudec and  
167 Jackson, 2004, Jackson and Hudec, 2008, Serié et al., 2017).

168 The second phase of significant post-salt extension occurred during the Neogene, triggered by  
169 onshore cratonic uplift (Jackson et al., 2005, Hudec and Jackson, 2004). Basement-involved  
170 uplift of the continental shelf and upper slope in the Miocene resulted in an increase in the rate  
171 of seaward translation of the salt and its overburden, from *c.* 0.2 to 1 mm/yr (Jackson and  
172 Hudec, 2008, Jackson et al., 2005, Hudec and Jackson, 2004, Evans and Jackson, 2019). This  
173 resulted in a further 20 km of extension in the Outer Kwanza Basin (Hudec and Jackson, 2003,  
174 Jackson and Hudec, 2008, Evans and Jackson, 2019). The faults we study likely form in  
175 response to this extensional phase. Since the Miocene, sedimentation in the Outer Kwanza  
176 Basin has been dominated by hemipelagic clays and silts, with coarser-grained sediments being  
177 deposited in the basin in turbidite-fed channels and lobes. Seismically chaotic MTCs, of  
178 unknown composition, are also observed in the post-Miocene sedimentary sequence (Serié et  
179 al., 2017, Howlett et al., 2020).

## 180 **4 Results**

181 The normal fault array studied here sits within the axis of a N-trending minibasin (Fig. 3 and  
182 4). The largest faults dip to the north and offset Tertiary stratigraphy (Fig. 3 and 4). The D-L  
183 data for the faults broadly fit within global D-L trend, sitting in the lower part of the dataset  
184 (Fig. 2). Within the fault array we are able to define three distinct fault groups based on their  
185 geometrical characteristics and inferred kinematic behaviour (Fig. 4).

### 186 *4.1 Planar faults (F1-F5)*

#### 187 *4.1.1 Observations*

188 Planar faults are developed in the north of the study area, striking E-W and dipping 54-58°  
189 (Fig. 4 and 5). Striking orthogonal to the trend of adjacent salt wall, all of the faults dip  
190 northwards, with the exception of a single antithetic fault that dips southward (F1). The faults  
191 are 750–950 m tall and have maximum trace lengths of 1.8–4 km (Fig. 9). The maximum throw

192 in this group is ~ 20 m, with the throw maxima occurring in Pliocene stratigraphy (Fig. 8 and  
193 10). The upper tips of the planar faults are located in Pliocene stratigraphy and their lower tips  
194 are located in Miocene stratigraphy (Fig. 5). F1 and F2 are quasi-elliptical, whereas F3 and F4  
195 are elliptical (Fig. 8 b - e). The throw maxima for F1 and F2 are located near their centres, with  
196 throw ultimately decreasing towards their tips (Fig. 8 b and c). In contrast, throw maxima for  
197 F3 and F4 are slightly offset towards their lower halves (Fig. 8 d and e). This difference in the  
198 position of throw maxima is reflected in the lower-tip throw gradients. F1 and F2 show a  
199 relatively low throw gradient of 0.01, whereas F3 and F4 display throw gradients that are an  
200 order of magnitude greater (i.e. 0.12 and 0.11, respectively). The aspect ratio for planar faults  
201 with a throw maximum occurring along the Top Miocene horizon (i.e. F3 and F4) ranges from  
202 3.5-5.2, whereas the ratio for those with a throw maximum in shallower, Pliocene stratigraphy  
203 is 2.7 (F1 and 2) (Figs 8 and 10). The lower tips of faults that exhibit relatively high aspect  
204 ratios ( $> 3.5$ ), and which have maximum throws of  $< 20$  m, are located at the top of a laterally  
205 extensive, seismically chaotic unit that we interpret as an MTC (F3 and F4; Fig. 11 a)  
206 (Moscardelli and Wood, 2008).

207 Only F1, which has the largest throw and shallowest upper tip of all the planar faults, is  
208 associated with growth strata. In this case, Pliocene growth strata have an EI of 1.2 (Fig. 10).  
209 Stratigraphic packages adjacent to all of the other faults in the planar fault group have  $EI < 1.1$   
210 making it difficult to determine if these structures were ever growth faults that breached the  
211 free surface, or whether they grew as so-called 'blind' structures (e.g. Baudon and Cartwright,  
212 2008, Jackson et al., 2017).

213

214            *4.1.2 Interpretation*

215    Their quasi-elliptical geometry, relatively low aspect ratio, and concentric throw distribution  
216    suggest F1 and F2 grew as mechanically unrestricted structures (cf. F3 and F4 below; see also  
217    Fig. 8) (Nicol et al., 1996). Figure 11a shows that the lower tips of F3 and F4 coincide with the  
218    MTC. Furthermore, these faults have aspect ratios greater than those of F1 and F2. Given that  
219    these relatively closely spaced faults formed in similar host rock in response to broadly similar  
220    driving stresses, one plausible interpretation for the greater aspect ratios of F3 and F4 is that  
221    their basal tips mechanically interacted with the MTC near the base of the faulted sequence.  
222    This could have resulted in their tips being pinned, inducing the preferential lengthening of  
223    these faults and thus giving rise to the development of relatively high aspect ratios (Fig. 9; 11a  
224    and 12). This interpretation is supported by the observation that the throw maxima for F3 and  
225    F4 are slightly offset towards their lower tips, and that lower-tip throw gradients are higher for  
226    these faults than F1 and F2 (Fig. 8d and e). These geometrical characteristics are consistent  
227    with enhanced strain accumulation in these areas as a function of vertical tip restriction during  
228    fault propagation (Fig. 8 and 12) (Wilkins and Gross, 2002).

229    *4.2 Bifurcating faults (F6-F7)*

230            *4.2.1 Observations*

231    These faults are the longest in the studied array (> 5 km). They are characterised by a single  
232    fault segment at depth and two segments within shallower stratigraphy (F6 and F7; Fig. 4; 5  
233    and 13). Bifurcating faults (F6 and F7) strike WNW-ESE and dip 54-60° northward (Fig. 4 and  
234    5). The bifurcating faults contrast with the planar faults in two key ways; (i) they have larger  
235    throws (> 30 m; Fig. 11); and (ii) their basal tips lie beneath rather than above the MTC (Fig.  
236    3 and 13).

237 F7 bifurcates upwards with a sub-horizontal, c. 1.2 km long branchline coinciding with the top  
238 of the MTC (Fig. 4; 5 and 13b). Maximum throw on F7 (c. 32 m) is also located near the top  
239 of the MTC and the throw gradient below the MTC is relatively low (0.08; Fig. 13b). The  
240 maximum down-dip height and trace length of F7 are 1.75 km and 6.4 km respectively,  
241 resulting in an aspect ratio of 3.6 (Fig. 9 and 13b).

242 At the structural level of the Pliocene, F6 consists of two parallel, overlapping fault segments  
243 separated by a narrow (~70 m) relay zone (Fig. 4 and 5). At depth these segments link and form  
244 a single fault surface (Fig. 4c; 5 and 13a). Similar to F7, the c. 1 km long, sub-horizontal  
245 branchline for the two upper segments of F6 coincides with the top of the MTC (Fig. 13a). In  
246 contrast to F7, the throw maximum for F6 occurs beneath (rather than above) the MTC, within  
247 Oligocene-Miocene stratigraphy (Fig. 13a). The distribution of throw on F6 defines a broad,  
248 U-shaped (depth) throw maximum that encircles the relay zone and its associated throw  
249 minimum, and which extends below the MTC and beneath the branchline (blue area; Fig. 13a).  
250 Relatively high throw gradients of up to c. 0.2 occur in the relay zone where the faults overlap  
251 (sharp transition from blue to white; Fig. 13a). F6 has a maximum down-dip height and length  
252 of 1.9 km and 6.3 km, respectively, resulting in an aspect ratio of 3.3.

#### 253 *4.2.2 Interpretation*

254 The position of the maximum throw on F7 at the top of the MTC suggests the fault: (i) nucleated  
255 at this structural level; and/or (ii) nucleated elsewhere, possibly within the shallower  
256 stratigraphy, with the position of maximum throw migrating downwards with time. Irrespective  
257 of where the fault nucleated, it was able to propagate through the MTC (Fig. 13b). This  
258 observation, coupled with the distinct decrease in throw and throw gradient immediately below  
259 the MTC, suggest that the MTC may have initially retarded downward or upward propagation  
260 of F7, causing strain to accumulate along the top of the MTC before the fault could propagate  
261 onward (Fig. 13b and 14a). We therefore suggest that in a similar way to F3 and F4, the tips of

262 smaller, precursor segments were initially vertically restricted along the top of the MTC (Fig.  
263 14a). However, unlike in the case of F3 and F4, the accumulation of additional displacement  
264 meant tip stresses around F7 became high enough to allow the fault to breach the MTC (Fig.  
265 14a) (Wilkins and Gross, 2002).

266 In contrast to F7, we suggest F6 nucleated below (rather than above) the MTC based on the  
267 fact that maximum throw on the structure occurs at least partly below the MTC (Fig. 13a).  
268 Having nucleated below the MTC, F6 was then able to propagate upwards towards and  
269 ultimately through the MTC, locally bifurcating as it did (Fig. 14b). The throw distribution  
270 presently observed on F6 is consistent with numerically modelled throw distributions where a  
271 bifurcating planar frontal segment is present (Fig. 13a) (Soliva et al., 2008). We therefore  
272 suggest that the high throw values broadly encircling the relay zone, which is also associated  
273 with relatively high throw gradients (0.2), are as a result of tip interaction between the  
274 overlapping shallow segments during bifurcation and upward growth (Fig. 13a and 14b)  
275 (Nicol et al., 1996, Soliva et al., 2008, Nicol et al., 2017).

#### 276 *4.3 Arcuate faults (A1-A9)*

##### 277 *4.3.1 Observations*

278 The group is characterised by faults defined by smooth, along-strike changes in their  
279 orientation, resulting in a bow-shaped, convex trace in map-view (Fig. 4). This group of faults  
280 are concentrated in the south of the study area, on the northern rim of a locally deep part of the  
281 minibasin on the west of the salt wall; this deep area is best-expressed at the Pliocene and  
282 Miocene structural level (Fig. 4a and b, respectively). Close to the salt wall these faults strike  
283 E-W, perpendicular to the salt-sediment interface, changing to a NE-SW strike  $\geq 2$  km away  
284 from the salt wall; this change in strike defines their plan-view geometry, with the faults  
285 following the overall shape of the deep part of the minibasin (Fig. 4a and b). Maximum throws

286 on arcuate faults decrease with increasing distance from the salt wall; for example, A4 has a  
287 maximum throw of 44 m, whereas A9 has a maximum throw of ~10 m at 0.8 km and 3.5 km  
288 distance from the salt wall, respectively (Fig. 15a; see also Fig. 4a and b). We also note that  
289 arcuate faults appear overdisplaced, achieving similar maximum throws at only 60-70% of the  
290 strike length of other fault types (Fig. 15b). For example, A3 is 2.6 km long and has c. 35 m  
291 maximum throw, whereas F6 has comparable throw (c. 38 m) but is significantly longer (6.3  
292 km) (Fig. 15b). Arcuate faults also have notably lower aspect ratios (i.e. 1.4-2.7) compared to  
293 the linked and planar faults (i.e. 2.7-5.2) (Fig. 9).

294 We can sub-divide the arcuate fault group based on the depth at which they occur, the  
295 detailed fault geometry, and the overall throw distribution. The first subgroup faults strike  
296 broadly E-W (i.e. similar to the overall trend of the fault array) and are present at greater  
297 depths (i.e. below -1900 m) than the second subgroup (A1-4; Fig. 4a - c). They exhibit  
298 down-dip heights of 1–1.9 km and maximum lengths of 1.5–4.7 km, yielding aspect ratios of  
299 1.4 – 2.4 (Fig. 9). The largest faults in this subgroup, A3 and A4, have maximum throw  
300 values of 36 and 44 m, respectively, and offset the MTC, whereas those with throws < 30 m  
301 do not (Fig. 11b and c; and Fig. 15).

302 The second subgroup occurs at a shallower depth, in post-Miocene stratigraphy (A5-9; Fig. 3  
303 and 4a). The upper tips of faults in this subgroup are located just 100 m beneath the seabed and  
304 they typically tip out ~150 m above the Top Miocene horizon (Fig. 16). Four faults in this  
305 subgroup dip towards the south, towards the centre of the deep part of the minibasin described  
306 above, whereas one dips to the north (Fig. 4). A5-9 have down-dip heights which range between  
307 400–670 m and maximum lengths of 930–1730 m, yielding aspect ratios of 2.1 – 3.9 (Fig. 9)  
308 The maximum throw on these faults are generally less than that observed on A1-4 (i.e.  
309 maximum throws of ~10 - 15 m; Fig. 15 a).

310           4.3.2 *Interpretations*

311   Based on the fact that the arcuate faults closely parallel the outer rim of the deep part of the  
312   minibasin (Fig. 4) we suggest they formed to accommodate outer arc-style bending and  
313   stretching of the minibasin-fill during differential subsidence (Fig. 16). We propose these faults  
314   became overdisplaced for two reasons. Firstly, the larger faults in the first subgroup (A1 - 4)  
315   terminate very near the salt-sediment interface suggesting that these faults became restricted  
316   laterally due to not being able to propagate into the weak salt (e.g. Tvedt et al., 2013). Thus,  
317   resulting in these faults becoming overdisplaced as throw accrual continues under laterally  
318   restricted tips. Secondly, the shallower second subgroup are more closely spaced than other  
319   faults within the extensional array and are sub-parallel (Fig. 4a). We propose that these faults  
320   experienced mechanical interactions between their fault tips, which resulted in lateral  
321   restriction of their growth and overdisplacement. While the cause (i.e fault interaction) for fault  
322   restriction differs to that of the larger arcuate faults (i.e. salt interaction), the result of  
323   overdisplacement is the same (e.g. Crider and Pollard, 1998, Martel, 1999, Nicol et al., 2017).

324   **5 Discussion and Implications**

325   *5.1 Origin and kinematics of planar normal faults; the case for tip restriction by host rock*  
326   *properties*

327   The occurrence of throw maxima within Miocene and Pliocene strata suggest the planar faults  
328   nucleated within Neogene stratigraphy (Fig. 10) (Hongxing and Anderson, 2007). Whereas all  
329   other planar faults propagated as blind structures, F1 represented a surface-breaching growth  
330   fault during at least the Pliocene (Fig. 10). During the Middle Miocene, salt and overburden  
331   translation rates increased significantly from *c.* 0.2 to 1 mm/yr within the Outer Kwanza Basin,  
332   principally due to margin uplift (Hudec and Jackson, 2004, Evans and Jackson, 2019).  
333   Depending on the structural position on the margin, this resulted in extensional (i.e. typically

334 in updip, proximal locations) or contractional (i.e. typically in downdip, distal locations)  
335 deformation of salt and its overburden (Hudec and Jackson, 2004, Evans and Jackson, 2019).  
336 Despite our study area being in the present-day transitional domain (Fig. 1), increases in  
337 downdip salt flux could have resulted in local extension of this area due to outer-arc bending  
338 and translation across the base-salt relief (Evans and Jackson, 2019). The planar faults may  
339 therefore have formed in the Middle Miocene in response to this increased rate of basinward  
340 translation of salt and its overburden, eventually breaching the seabed in the Pliocene, as  
341 evidenced by the presence of the growth strata in the hanging wall of F1 (Evans and Jackson,  
342 2019).

343 Field-based studies and modelling results show that mechanical stratigraphy can influence the  
344 growth and ultimate geometry of normal faults; e.g. multi-layered sequences defined by  
345 different rock competencies controls, down-dip linkage, fault restriction and fault aspect ratio  
346 (e.g. Wilkins and Gross, 2002, Soliva and Benedicto, 2005, Schöpfer et al., 2006). For example,  
347 Nicol et al. (1996) suggest vertically restricted faults display greater aspect ratios. More recent  
348 work proposes various mechanisms by which vertical restriction might occur, showing that  
349 faults growing in mechanically more homogenous host rocks assume circular to elliptical  
350 shapes throughout their lives, whereas those in multi-layered sequences can have their vertical  
351 growth impeded, thus growing from a circular to an elliptical geometry, resulting in an increase  
352 in aspect ratio (Fig. 12) (Soliva et al., 2005a, Soliva and Benedicto, 2005, Soliva et al., 2006).  
353 One consequence of the latter style of fault growth is the development of high throw gradients  
354 at the restricted (vertical) tip (Fig. 8d and e) (Wilkins and Gross, 2002). Within the planar fault  
355 group, F3 and F4 have relatively high aspect ratios (3.5 and 5.2, respectively) and high throw  
356 gradients (0.12 and 0.11, respectively) at their lower tips; these values are an order-of-  
357 magnitude greater than those of F1 and F2 (0.01). The migration of throw to the restricted tip  
358 and consequent high throw gradients is shown by the presence of their throw maxima being

359 slightly offset towards their lower tips, which is characteristic of mechanically bound faults  
360 (Fig. 8 d and e; and 10) (e.g. Wilkins and Gross, 2002, Soliva and Benedicto, 2005, Soliva et  
361 al., 2005b). In contrast, relatively closely ( $< 1$  km) spaced faults within the bifurcating fault  
362 group, which have throw maxima of  $> 30$  m and that offset the MTC, do not have these  
363 geometric characteristics (Fig. 11). This pattern, where only faults with  $T_{\max} > 30$  m offset the  
364 MTC, can be observed in the arcuate fault group in the extensional array (Fig. 11b). An  
365 important observation is that, despite being  $< 1$  km from F3 and 4 and although they offset  
366 similar stratigraphy (Fig. 5), the lower tips of F1 and 2 lie above the MTC; as a result, these  
367 faults do not have the same high aspect ratios or throw gradients at their lower tips (Fig. 5; 7  
368 and 9).

369 The variable geometric relationships between the faults and the MTC suggests that it acted as  
370 a mechanical layer, restricting the downward and upward propagation of the fault tips and  
371 overall enlargement of the surfaces of faults that ultimately only accumulated only  $< 30$  m  
372 maximum throw (Fig. 11 b). This resulted in higher aspect ratios and lower tip throw gradients  
373 on those faults not able to propagate, as well as influencing the growth, geometry and throw  
374 distribution of bifurcating faults (Fig. 12 and 14). Because drilling data are not available to  
375 determine the MTC lithology or mechanical properties, we do not know if this unit retarded tip  
376 propagation by: (i) acting as a relatively stiff layer that was hard to strain; or (ii) acting in a  
377 ductile manner, with strain being internally distributed in more diffuse manner. The latter case  
378 has been observed in field-based studies of normal faulted, mechanically layered host rocks,  
379 with faults seemingly nucleating and propagating only in more competent, stiff layers (typically  
380  $>0.5$  m thick) (Soliva et al., 2005b). Underlying and overlying, more compliant layers ( $<0.5$  m  
381 thick) behave in a ductile manner and are characterised by diffuse strain and high strain  
382 gradients. Faults essentially decouple in these layers, with high aspect ratios and  
383 underdisplaced fault populations arising as a function of 'forced' propagation within the stiff

384 layers. We propose that this case may also apply at a substantially larger, seismic-scale, such  
385 as that documented here. Deep water MTC's are predominantly mudstone-dominated (Wu et  
386 al., 2019) meaning that it could be the case that they act in a ductile manner with strain being  
387 more diffuse, as documented in mechanically heterogeneous faulted sequences (e.g. Bürgmann  
388 et al., 1994, e.g. Nicol et al., 1996, Wilkins and Gross, 2002, Soliva and Benedicto, 2005,  
389 Soliva et al., 2005b, Soliva et al., 2005a, Roche et al., 2012). In the absence of drilling data,  
390 we propose that either of these hypotheses could be the case for the MTC's mechanical control  
391 on fault growth.

## 392 *5.2 Kinematics of bifurcating faults; overcoming tip restriction and continued fault growth*

393 Fault linkage and bifurcation control throw distributions on normal fault surfaces (Peacock and  
394 Sanderson, 1991, Dawers and Anders, 1995, Mansfield and Cartwright, 2001, Peacock, 2002,  
395 Soliva and Benedicto, 2004, Soliva et al., 2008). We noted that the laterally restricted  
396 branchline of F7 occurs at the top of the Miocene MTC, and that the throw maximum also lies  
397 at this structural and stratigraphic level. The throw maximum is restricted to the larger,  
398 rearward (i.e. footwall side) fault and does not continue onto the frontal (i.e. hangingwall side)  
399 splay (Fig. 13b). In section 5.1 we discussed that the vertical restriction of the lower tips within  
400 the planar fault group resulted in high throw gradients (Wilkins and Gross, 2002, Jackson et  
401 al., 2014). If a similar process occurred during growth of the bifurcating fault F7, it could follow  
402 that pinned precursor segments concentrated stress at their lower tips before linking and  
403 propagating onward, creating the present throw pattern (Fig. 13b and 14a). The same process  
404 could occur for a segmented fault system nucleating below and ultimately propagating upwards  
405 through a mechanical layer (Wilkins and Gross, 2002).

406 Bifurcating fault F6 shows a distinct concentration of high throw near the MTC (Fig. 13a); this  
407 is consistent with the hypothesis of stress and strain concentration at the MTC prior to onward

408 fault propagation (Fig. 14). Moreover, a second distinct area of high throw occurs on the frontal  
409 fault of F6, immediately east of the relay zone (Fig. 13a); this is consistent with throw  
410 distributions typically seen within relay zones, where tip interaction occurs between adjacent,  
411 upward-propagating segments (Peacock and Sanderson, 1991, Trudgill and Cartwright, 1994,  
412 Peacock and Sanderson, 1994, Peacock, 2002, Long and Imber, 2012, Freitag et al., 2017).  
413 Fault bifurcation can occur as a result of stress field reorientation or non-uniformity, as well as  
414 irregular tip-line propagation due to intra-host rock mechanical heterogeneities, such as an  
415 intra-stratal MTC (Soliva et al., 2008). This would explain the bifurcation and position of the  
416 branchline on the top of the MTC (Fig. 5a and 13). Our data suggest that only faults that  
417 accumulated > 30 m of throw were able to propagate through the MTC; below this value, the  
418 tips were pinned due to the build-up of insufficient tip stresses to allow onward propagation  
419 (Fig. 11 a and b) (Wilkins and Gross, 2002).

### 420 *5.3 Normal fault growth and D-L scaling relationships*

421 D-L scaling relationships derived from global datasets have historically been used to support a  
422 normal fault growth model by synchronous lengthening and displacement accumulation (i.e.  
423 'propagating model'; Childs et al., 2017, Rotevatn et al., 2018); (See also e.g. Watterson, 1986,  
424 Walsh and Watterson, 1988, Walsh et al., 2002). More recently, however, studies using 3D  
425 seismic reflection data have integrated stratigraphic data in an otherwise purely geometrical  
426 analyses; this has given rise to an alternative fault growth model that states fault lengthening  
427 (which may include linkage of initially isolated segments) occurs before the accumulation of  
428 significant displacement (i.e. 'constant-length model'; Jackson and Rotevatn, 2013, Childs et  
429 al., 2017, Rotevatn et al., 2019, Nicol et al., 2020).

430 We show here that host-rock heterogeneities, and near- and far-field stress regimes and their  
431 interactions, can all result in the formation of under- or over-displaced faults (i.e. faults that

432 significantly deviate from global D-L scaling relationships and thus produce scatter within  
433 these datasets), and/or faults with anomalously low or high aspect ratios (Cowie and Scholz,  
434 1992a, Dawers and Anders, 1995, Peacock, 2002, Soliva and Benedicto, 2005, Soliva et al.,  
435 2005b, Soliva et al., 2005a). This is in addition to fault linkage, which typically results in  
436 underdisplaced faults likely characterised by anomalously low aspect ratios (Cartwright et al.,  
437 1995). Our study shows how detailed analysis of largely blind faults of varying sizes  
438 developing within the same overall tectono-stratigraphic setting can shed light on the  
439 kinematics of fault growth; such studies can complement those focused on growth faults  
440 flanked by syn-kinematic strata (e.g. Tvedt et al., 2013, Duffy et al., 2015, e.g. Jackson et al.,  
441 2017). A key observation is that the studied faults would fall within the general scatter present  
442 in global D-L scaling datasets (Fig. 2), and that this would mask the not insignificant variability  
443 in their geometric properties (i.e. D-L relationship, aspect ratio) and inferred growth patterns,  
444 and the relationship of these to local stratigraphic factors (i.e. an intra-stratal MTC).

## 445 **6.0 Conclusions**

446 By conducting a detailed analysis of fault aspect ratio, throw distribution patterns, and post-  
447 depositional fault interaction within a mechanical medium, fault behaviour and growth can be  
448 deduced (Watterson, 1986, Walsh and Watterson, 1987, Marrett and Allmendinger, 1990,  
449 Cowie and Scholz, 1992a, Bürgmann et al., 1994, Gupta and Scholz, 2000, Jackson et al.,  
450 2017). Several factors have been identified which appear to control the propagation of normal  
451 faults and the magnitude and distribution of displacement across the fault surface (Willemse et  
452 al., 1996, Schultz, 1999, Soliva and Benedicto, 2005, Soliva and Schultz, 2008). These include  
453 fault geometry, mechanical and rheological properties of the medium (Schultz, 1999), near-  
454 and far-field stress regimes, and fault linkage (Soliva and Benedicto, 2004, Lohr et al., 2008,  
455 Rotevatn et al., 2018):

- 456 • Mechanical boundary layers (i.e. an intra-stratal MTC) can inhibit onward fault  
457 propagation and create vertically restricted faults on much larger faults than previously  
458 observed, as shown in this study where seismic scale faults grew vertically restricted.  
459 A comparison of unrestricted and restricted faults (F1-2 and F3-4, respectively)  
460 displays this relationship where aspect ratios for unrestricted faults was 2.7 while  
461 restricted faults range from 3.7-5.2 (Fig. 8). Where faults are restricted and do not  
462 achieve critical tip stresses for onward growth by offsetting the mechanical layer, their  
463 growth is dominated by preferential lengthening as in the case of F3 and F4 (Fig. 9 and  
464 12). Furthermore, where faults grow in this way, the throw maximum migrates towards  
465 the restricting layer as stress accumulation occurs at the fault tips (Fig. 8 d and e) and  
466 results in relatively high throw gradients at the restricted tip; as observed on F3-4 which  
467 manifested tip throw gradients of 0.12 and 0.11, respectively. In this case, representing  
468 throw gradients an order of magnitude greater than those observed on unrestricted fault  
469 tips (Fig. 8).
- 470 • Stress accumulation and segment linkage allows for the accumulation of length and tip  
471 stresses, such that it facilitates previously pinned precursor faults to overcome critical  
472 tip stresses; i.e. where maximum throw > 30 m (Fig. 11), and achieve onward growth  
473 beyond the vertically restricting layer (Fig. 11 and 14). On faults which overcome  
474 vertical restricting layers, throw maxima persist on the fault surface at the structural  
475 level of the previously restricting layer (Fig. 13). Thus, maintaining the position of the  
476 throw maximum established during immature stages of growth which migrated towards  
477 the restricting layer, in a manner not dissimilar to the suggested throw behaviour of F3-  
478 4 (Fig. 8 d and e). This is most clearly highlighted on F7 where the throw maximum is  
479 located along the Top MTC surface (Fig. 13 b).

480 • The arcuate fault group highlights well our initial hypothesis that faults can deviate  
481 from D-L scaling laws as they grow, even when they presently have D-L scaling  
482 relationship that adhere to global compilations ( $D = cL^n$ ; Fig. 2). These fault were  
483 overdisplaced achieving similar maximum throws to other faults at 60-70% of the strike  
484 length of other fault types (Fig. 15 b). While these faults deviate from expected D-L  
485 relationships within the studied finite array, all of these faults sit within global D-L data  
486 scatter (Fig. 2). Furthermore, our study of planar and bifurcated fault groups and their  
487 interactions with mechanical medium, highlights that D-L scaling (i.e. geometric) data  
488 alone does not allow us to determine the style of fault growth; as often used in the  
489 discussion of fault growth models, as these too sit within D-L scaling data scatter  
490 masking their complexity (Fig. 2). Therefore, fault growth and D-L scaling  
491 relationships must be considered within the context of local mechanical stratigraphy,  
492 stress-fields and fault interaction. Furthermore, the analysis of faults of varying scales  
493 within a single population, can together provide more robust kinematic constraints in  
494 order to adequately determine fault growth models and determine the D-L relationship  
495 across scales of fault growth. Such an approach can highlight fault growth histories  
496 otherwise masked within static D-L datasets.

## 497 **Acknowledgements**

498 We thank the NERC Centre for Doctoral Training in Oil and Gas for the provision of funding  
499 to the PhD research of David Redpath. We also thank CGG for their continued commitment to  
500 quality data. The dataset can be found by contacting CGG. We also thank Schlumberger for  
501 providing access to Petrel software.

502

503 ATHMER, W. & LUTHI, S. M. 2011. The effect of relay ramps on sediment routes and  
504 deposition: A review. *Sedimentary Geology*, 242, 1-17.

- 505 BATE, R. H., CAMERON, N. R. & BRANDÃO, M. G. P. 2001. The lower cretaceous (Pre-  
506 Salt) lithostratigraphy of the Kwanza Basin, Angola, *Newsletter on Stratigraphy*, 38,  
507 117-127.
- 508 BAUDON, C. & CARTWRIGHT, J. 2008. The kinematics of reactivation of normal faults  
509 using high resolution throw mapping. *Journal of Structural Geology*, 30, 1072-1084.
- 510 BODVARSSON, G., BENSON, S. & WITHERSPOON, P. 1982. Theory of the development  
511 of geothermal systems charged by vertical faults. *Journal of Geophysical Research:*  
512 *Solid Earth*, 87, 9317-9328.
- 513 BRICE, S. E., COCHRAN, M. D., PARDO, G. & EDWARDS, A. D. 1982. Tectonics and  
514 Sedimentation of the South Atlantic Rift Sequence: Cabinda, Angola. *AAPG Memoirs*,  
515 34. Studies in Continental Margin Geology. In: WATKINS, J. S. & DRAKE, C. L.  
516 (eds.).
- 517 BÜRGMANN, R., POLLARD, D. D. & MARTEL, S. J. 1994. Slip distributions on faults:  
518 effects of stress gradients, inelastic deformation, heterogeneous host-rock stiffness, and  
519 fault interaction. *Journal of Structural Geology*, 16, 1675-1690.
- 520 CARTWRIGHT, J. A., TRUDGILL, B. D. & MANSFIELD, C. S. 1995. Fault growth by  
521 segment linkage: an explanation for scatter in maximum displacement and trace length  
522 data from the Canyonlands Grabens of SE Utah. *Journal of Structural Geology*, 17,  
523 1319-1326.
- 524 CHILDS, C., HOLDSWORTH, R. E., JACKSON, C. A. L., MANZOCCHI, T., WALSH, J. J.  
525 & YIELDING, G. 2017. Introduction to the geometry and growth of normal faults.  
526 *Geological Society, London, Special Publications*, 439, 1.
- 527 CHILDS, C., NICOL, A., WALSH, J. J. & WATTERSON, J. 2003. The growth and  
528 propagation of synsedimentary faults. *Journal of Structural Geology*, 25, 633-648.
- 529 COLLANEGA, L., JACKSON, C., BELL, R., COLEMAN, A., LENHART, A. & BREDA, A.  
530 2018. Normal fault growth influenced by basement fabrics: the importance of  
531 preferential nucleation from pre-existing structures. *Basin Research*, 31, 659-687
- 532 CORBEL, S., SCHILLING, O., HOROWITZ, F., REID, L., SHELDON, H., TIMMS, N. &  
533 WILKES, P. Identification and geothermal influence of faults in the Perth metropolitan  
534 area, Australia. *Thirty-Seventh Workshop on Geothermal Reservoir Engineering, 2012.*  
535 *Stanford University California*, 8.
- 536 COWIE, P. A. & SCHOLZ, C. H. 1992a. Displacement-length scaling relationship for faults:  
537 data synthesis and discussion. *Journal of Structural Geology*, 14, 1149-1156.
- 538 COWIE, P. A. & SCHOLZ, C. H. 1992b. Growth of faults by accumulation of seismic slip.  
539 *Journal of Geophysical Research: Solid Earth*, 97, 11085-11095.
- 540 CRIDER, J. G. & POLLARD, D. D. 1998. Fault linkage: Three-dimensional mechanical  
541 interaction between echelon normal faults. *Journal of Geophysical Research: Solid*  
542 *Earth*, 103, 24373-24391.
- 543 DAWERS, N. H. & ANDERS, M. H. 1995. Displacement-length scaling and fault linkage.  
544 *Journal of Structural Geology*, 17, 607-614.
- 545 DUFFY, O., BELL, R., JACKSON, C., L. GAWTHORPE, R. & S. WHIPP, P. 2015. Fault  
546 Growth and Interactions in a Multiphase Rift Fault Network: Horda Platform,  
547 Norwegian North Sea, *Journal of Structural Geology*, 80, 99-119.
- 548 ELIET, P. & GAWTHORPE, R. 1995. Drainage development and sediment supply within rifts,  
549 examples from the Sperchios basin, central Greece. *Journal of the Geological Society*,  
550 152, 883-893.
- 551 EVANS, S. L. & JACKSON, C. A.-L. 2019. Base-salt relief controls salt-related deformation  
552 in the Outer Kwanza Basin, offshore Angola. *Basin Research*, 32, 668-687.

553 FAIRLEY, J. P. & HINDS, J. J. 2004. Rapid transport pathways for geothermal fluids in an  
554 active Great Basin fault zone. *Geology*, 32, 825-828.

555 FREITAG, U. A., SANDERSON, D. J., LONERGAN, L. & BEVAN, T. G. 2017. Comparison  
556 of upwards splaying and upwards merging segmented normal faults. *Journal of*  
557 *Structural Geology*, 100, 1-11.

558 GAWTHORPE, R. L. & HURST, J. M. 1993. Transfer zones in extensional basins: their  
559 structural style and influence on drainage development and stratigraphy. *Journal of the*  
560 *Geological Society*, 150, 1137-1152.

561 GAWTHORPE, R. L. & LEEDER, M. R. 2000. Tectono-sedimentary evolution of active  
562 extensional basins. *Basin Research*, 12, 195-218.

563 GHALAYINI, R., DANIEL, J.-M., NADER, F. & HOMBERG, C. 2016. Predicting reservoir  
564 intervals by looking at fault data: An exploration tool in frontier basins. *International*  
565 *Conference and Exhibition, Barcelona, Spain, 3-6 April 2016*.

566 GIBBS, A. D. 1984. Structural evolution of extensional basin margins. *Journal of the*  
567 *Geological Society*, 141, 609-620.

568 GUPTA, A. & SCHOLZ, C. H. 2000. A model of normal fault interaction based on  
569 observations and theory. *Journal of Structural Geology*, 22, 865-879.

570 HONGXING, G. & ANDERSON, J. K. 2007. Fault throw profile and kinematics of Normal  
571 fault: conceptual models and geologic examples. *Geological Journal of China*  
572 *Universities*, 13, 75-88.

573 HOWLETT, D. M., GAWTHORPE, R. L., GE, Z., ROTEVATN, A. & JACKSON, C. A.-L.  
574 2020. Turbidites, topography and tectonics: Evolution of submarine channel-lobe  
575 systems in the salt-influenced Kwanza Basin, offshore Angola. *Basin Research*.

576 HUDEC, M. & JACKSON, M. 2003. Structural segmentation, inversion, and salt tectonics on  
577 a passive margin: Evolution of the Inner Kwanza Basin, Angola. *The Geological*  
578 *Society of America Bulletin*, 115, 641.

579 HUDEC, M. & JACKSON, M. 2004. Regional restoration across the Kwanza Basin, Angola:  
580 Salt tectonics triggered by repeated uplift of a metastable passive margin. *AAPG*  
581 *Bulletin*, 88,971-990.

582 JACKSON, C. A.-L., CARRUTHERS, D. T., MAHLO, S. N. & BRIGGS, O. 2014. Can  
583 polygonal faults help locate deep-water reservoirs? *AAPG Bulletin*, 98, 1717-1738.

584 JACKSON, C. A. L., BELL, R. E., ROTEVATN, A. & TVEDT, A. B. M. 2017. Techniques  
585 to determine the kinematics of synsedimentary normal faults and implications for fault  
586 growth models. *Geological Society, London, Special Publications*, 439, 187.

587 JACKSON, C. A. L. & ROTEVATN, A. 2013. 3D seismic analysis of the structure and  
588 evolution of a salt-influenced normal fault zone: A test of competing fault growth  
589 models. *Journal of Structural Geology*, 54, 215-234.

590 JACKSON, M. P. A. & HUDEC, M. R. 2008. Interplay of Basement, Salt Tectonics, and  
591 Sedimentation in the Kwanza Basin, Angola *AAPG International Conference and*  
592 *Exhibition 2008*.

593 JACKSON, M. P. A., HUDEC, M. R. & HEGARTY, K. A. 2005. The great West African  
594 Tertiary coastal uplift: Fact or fiction? A perspective from the Angolan divergent  
595 margin. *Tectonics*, 24, 6.

596 KARNER, G. D. & GAMBÔA, L. A. P. 2007. Timing and origin of the South Atlantic pre-salt  
597 sag basins and their capping evaporites. *Geological Society, London, Special*  
598 *Publications*, 285, 15.

599 KHALIL, S. M. & MCCLAY, K. R. 2017. 3D geometry and kinematic evolution of extensional  
600 fault-related folds, NW Red Sea, Egypt. *Geological Society, London, Special*  
601 *Publications*, 439, 109.

- 602 LEEDER, M. R. & GAWTHORPE, R. L. 1987. Sedimentary models for extensional tilt-  
603 block/half-graben basins. *Geological Society, London, Special Publications*, 28, 139-  
604 152.
- 605 LOHR, T., M. KRAWCZYK, C., ONCKEN, O. & TANNER, D. 2008. Evolution of a fault  
606 surface from 3D attribute analysis and displacement measurements. *Journal of*  
607 *Structural Geology*, 30, 690-700.
- 608 LONG, J. J. & IMBER, J. 2012. Strain compatibility and fault linkage in relay zones on normal  
609 faults. *Journal of Structural Geology*, 36, 16-26.
- 610 MANSFIELD, C. & CARTWRIGHT, J. 2001. Fault growth by linkage: Observations and  
611 implications from analogue models. *Journal of Structural Geology*, 23, 745-763.
- 612 MARRETT, R. & ALLMENDINGER, R. W. 1990. Kinematic analysis of fault-slip data.  
613 *Journal of Structural Geology*, 12, 973-986.
- 614 MARTEL, S. J. 1999. Mechanical controls on fault geometry. *Journal of Structural Geology*,  
615 21, 585-596.
- 616 MARTON, L. G., TARI, G. C. & LEHMANN, C. T. 2000. Evolution of the Angolan passive  
617 margin, West Africa, with emphasis on post-salt structural styles. *Geophysical*  
618 *Monograph-American Geophysical Union*, 115, 129-150.
- 619 MCCLAY, K. R. 1990. Extensional fault systems in sedimentary basins: a review of analogue  
620 model studies. *Marine and Petroleum Geology*, 7, 206-233.
- 621 MCLEOD, A. E., DAWERS\*, N. H. & UNDERHILL, J. R. 2000. The propagation and linkage  
622 of normal faults: insights from the Strathspey–Brent–Statfjord fault array, northern  
623 North Sea. *Basin Research*, 12, 263-284.
- 624 MORLEY, C. 2017. The impact of multiple extension events, stress rotation and inherited  
625 fabrics on normal fault geometries and evolution in the Cenozoic rift basins of Thailand.  
626 *Geological Society, London, Special Publications*, 439, 413-445.
- 627 MORLEY, C. K. 2007. Development of crestal normal faults associated with deepwater fold  
628 growth. *Journal of Structural Geology*, 29, 1148-1163.
- 629 MOSCARDELLI, L. & WOOD, L. 2008. New classification system for mass transport  
630 complexes in offshore Trinidad. *Basin Research*, 20, 73-98.
- 631 NICOL, A., CHILDS, C., WALSH, J., MANZOCCHI, T. & SCHÖPFER, M. 2017.  
632 Interactions and growth of faults in an outcrop-scale system. *Geological Society,*  
633 *London, Special Publications*, 439, 23-39.
- 634 NICOL, A., WALSH, J., BERRYMAN, K. & NODDER, S. 2005. Growth of a normal fault  
635 by the accumulation of slip over millions of years. *Journal of Structural Geology*, 27,  
636 327-342.
- 637 NICOL, A., WALSH, J., CHILDS, C. & MANZOCCHI, T. 2020. Chapter 6 - The growth of  
638 faults. In: TANNER, D. & BRANDES, C. (eds.) *Understanding Faults*. Elsevier.
- 639 NICOL, A., WATTERSON, J., WALSH, J. J. & CHILDS, C. 1996. The shapes, major axis  
640 orientations and displacement patterns of fault surfaces. *Journal of Structural Geology*,  
641 18, 235-248.
- 642 PEACOCK, D. & SANDERSON, D. 1994. Geometry and development of relay ramps in  
643 normal fault systems. *AAPG bulletin*, 78, 147-165.
- 644 PEACOCK, D. C. P. 2002. Propagation, interaction and linkage in normal fault systems. *Earth-*  
645 *Science Reviews*, 58, 121-142.
- 646 PEACOCK, D. C. P. & SANDERSON, D. J. 1991. Displacements, segment linkage and relay  
647 ramps in normal fault zones. *Journal of Structural Geology*, 13, 721-733.
- 648 POLIT, A. T., SCHULTZ, R. A. & SOLIVA, R. 2009. Geometry, displacement–length scaling,  
649 and extensional strain of normal faults on Mars with inferences on mechanical  
650 stratigraphy of the Martian crust. *Journal of Structural Geology*, 31, 662-673.

- 651 REEVE, M. T., BELL, R. E., DUFFY, O. B., JACKSON, C. A.-L. & SANSOM, E. 2015. The  
652 growth of non-colinear normal fault systems; What can we learn from 3D seismic  
653 reflection data? *Journal of Structural Geology*, 70, 141-155.
- 654 REILLY, C., NICOL, A., WALSH, J. J. & KROEGER, K. F. 2016. Temporal changes of fault  
655 seal and early charge of the Maui Gas-condensate field, Taranaki Basin, New Zealand.  
656 *Marine and Petroleum Geology*, 70, 237-250.
- 657 ROCHE, V., HOMBERG, C. & ROCHER, M. 2012. Fault displacement profiles in multilayer  
658 systems: from fault restriction to fault propagation. *Terra Nova*, 24, 499-504.
- 659 ROTEVATN, A., FOSSEN, H., HESTHAMMER, J., AAS, T. E. & HOWELL, J. A. 2007.  
660 Are relay ramps conduits for fluid flow? Structural analysis of a relay ramp in Arches  
661 National Park, Utah. *Geological Society, London, Special Publications*, 270, 55.
- 662 ROTEVATN, A., JACKSON, C. A. L., TVEDT, A. B. M., BELL, R. E. & BLÆKKAN, I.  
663 2018. How do normal faults grow? *Journal of Structural Geology*.
- 664 ROTEVATN, A., JACKSON, C. A. L., TVEDT, A. B. M., BELL, R. E. & BLÆKKAN, I.  
665 2019. How do normal faults grow? *Journal of Structural Geology*, 125, 174-184.
- 666 SCHÖPFER, M. P. J., CHILDS, C. & WALSH, J. J. 2006. Localisation of normal faults in  
667 multilayer sequences. *Journal of Structural Geology*, 28, 816-833.
- 668 SCHULTZ, R. 1999. Understanding the process of faulting: selected challenges and  
669 opportunities at the edge of the 21st century. *Journal of Structural Geology*, 21, 985-  
670 993.
- 671 SERIÉ, C., HUUSE, M., SCHØDT, N. H., BROOKS, J. M. & WILLIAMS, A. 2017.  
672 Subsurface fluid flow in the deep-water Kwanza Basin, offshore Angola. *Basin*  
673 *Research*, 29, 149-179.
- 674 SOLIVA, R. & BENEDICTO, A. 2004. A linkage criterion for segmented normal faults.  
675 *Journal of Structural Geology*, 26, 2251-2267.
- 676 SOLIVA, R. & BENEDICTO, A. 2005. Geometry, scaling relations and spacing of vertically  
677 restricted normal faults. *Journal of Structural Geology*, 27, 317-325.
- 678 SOLIVA, R., BENEDICTO, A., SCHULTZ, R. A., MAERTEN, L. & MICARELLI, L. 2008.  
679 Displacement and interaction of normal fault segments branched at depth: Implications  
680 for fault growth and potential earthquake rupture size. *Journal of Structural Geology*,  
681 30, 1288-1299.
- 682 SOLIVA, R., BENEDICTO, A., VERGÉLY, P. & RIVES, T. 2005a. Mechanical control of a  
683 lithological alternation on normal fault morphology, growth and reactivation. *Bulletin*  
684 *de la Société Géologique de France*, 176, 329-342.
- 685 SOLIVA, R. & SCHULTZ, R. A. 2008. Distributed and localized faulting in extensional  
686 settings: insight from the North Ethiopian Rift–Afar transition area. *Tectonics*, 27.
- 687 SOLIVA, R., SCHULTZ, R. A. & BENEDICTO, A. 2005b. Three-dimensional displacement-  
688 length scaling and maximum dimension of normal faults in layered rocks. *Geophysical*  
689 *Research Letters*, 32.
- 690 SOLIVA, S., ANTONIO, B. & LAURENT, M. 2006. Spacing and linkage of confined normal  
691 faults: Importance of mechanical thickness. *Journal of Geophysical Research: Solid*  
692 *Earth*, 111.
- 693 SPATHOPOULOS, F. 1996. An insight on salt tectonics in the Angola Basin, South Atlantic.  
694 *Geological Society, London, Special Publications*, 100, 153.
- 695 TORABI, A., ALAEI, B. & LIBAK, A. 2019. Normal fault 3D geometry and displacement  
696 revisited: Insights from faults in the Norwegian Barents Sea. *Marine and Petroleum*  
697 *Geology*, 99, 135-155.
- 698 TRUDGILL, B. D. & CARTWRIGHT, J. A. 1994. Relay-ramp forms and normal-fault  
699 linkages, Canyonlands National Park, Utah. *GSA Bulletin*, 106, 1143-1157.

- 700 TVEDT, A. B. M., ROTEVATN, A. & JACKSON, C. A. L. 2016. Supra-salt normal fault  
701 growth during the rise and fall of a diapir: Perspectives from 3D seismic reflection data,  
702 Norwegian North Sea. *Journal of Structural Geology*, 91, 1-26.
- 703 TVEDT, A. B. M., ROTEVATN, A., JACKSON, C. A. L., FOSSEN, H. & GAWTHORPE,  
704 R. L. 2013. Growth of normal faults in multilayer sequences: A 3D seismic case study  
705 from the Egersund Basin, Norwegian North Sea. *Journal of Structural Geology*, 55, 1-  
706 20.
- 707 WALSH, J. J., BAILEY, W. R., CHILDS, C., NICOL, A. & BONSON, C. G. 2003. Formation  
708 of segmented normal faults: a 3-D perspective. *Journal of Structural Geology*, 25,  
709 1251-1262.
- 710 WALSH, J. J., NICOL, A. & CHILDS, C. 2002. An alternative model for the growth of faults.  
711 *Journal of Structural Geology*, 24, 1669-1675.
- 712 WALSH, J. J. & WATTERSON, J. 1987. Distributions of cumulative displacement and  
713 seismic slip on a single normal fault surface. *Journal of Structural Geology*, 9, 1039-  
714 1046.
- 715 WALSH, J. J. & WATTERSON, J. 1988. Analysis of the relationship between displacements  
716 and dimensions of faults. *Journal of Structural Geology*, 10, 239-247.
- 717 WALSH, J. J. & WATTERSON, J. 1991. Geometric and kinematic coherence and scale effects  
718 in normal fault systems. *Geological Society, London, Special Publications*, 56, 193-  
719 203.
- 720 WATTERSON, J. 1986. Fault dimensions, displacements and growth. *Pure And Applied*  
721 *Geophysics*, 124, 365-373.
- 722 WHIPP, P., JACKSON, C. L., GAWTHORPE, R., DREYER, T. & QUINN, D. 2014. Normal  
723 fault array evolution above a reactivated rift fabric; a subsurface example from the  
724 northern Horda Platform, Norwegian North Sea. *Basin Research*, 26, 523-549.
- 725 WILKINS, S. J. & GROSS, M. R. 2002. Normal fault growth in layered rocks at Split  
726 Mountain, Utah: influence of mechanical stratigraphy on dip linkage, fault restriction  
727 and fault scaling. *Journal of Structural Geology*, 24, 1413-1429.
- 728 WILKINSON, M., ROBERTS, G. P., MCCAFFREY, K., COWIE, P. A., FAURE WALKER,  
729 J. P., PAPANIKOLAOU, I., PHILLIPS, R. J., MICHETTI, A. M., VITTORI, E.,  
730 GREGORY, L., WEDMORE, L. & WATSON, Z. K. 2015. Slip distributions on active  
731 normal faults measured from LiDAR and field mapping of geomorphic offsets: an  
732 example from L'Aquila, Italy, and implications for modelling seismic moment release.  
733 *Geomorphology*, 237, 130-141.
- 734 WILLEMSE, E. J., POLLARD, D. D. & AYDIN, A. 1996. Three-dimensional analyses of slip  
735 distributions on normal fault arrays with consequences for fault scaling. *Journal of*  
736 *Structural Geology*, 18, 295-309.
- 737 WORTHINGTON, R. P. & WALSH, J. J. 2017. Timing, growth and structure of a reactivated  
738 basin-bounding fault. *Geological Society, London, Special Publications*, 439, 511.
- 739 WU, N., JACKSON, C., JOHNSON, H. & HODGSON, D. 2019. Lithological, petrophysical  
740 and seal properties of mass-transport complexes (MTCs), northern Gulf of Mexico.  
741 *Basin Research*, 32, 1300-1327.
- 742 XU, S., SAMANIEGO, Á. F. N., ÁLVAREZ, S. A. A. & MARTÍNEZ, L. M. C. 2011.  
743 Structural analysis of a relay ramp in the Querétaro graben, central Mexico:  
744 Implications for relay ramp development. *Revista mexicana de ciencias geológicas*, 28,  
745 275-289.
- 746 YOUNG, M. J., GAWTHORPE, R. L. & HARDY, S. 2001. Growth and linkage of a  
747 segmented normal fault zone; the Late Jurassic Murchison–Statfjord North Fault,  
748 northern North Sea. *Journal of Structural Geology*, 23, 1933-1952.

750 **Figure 1:** (Top left) A location map of the CGG 3D PDSM survey showing the 70 km<sup>2</sup> study  
751 area and the regional section. (Top right) A seafloor depth structure map highlighting the  
752 presence of the N-S trending salt wall and the minibasin on its western flank, which characterise  
753 our study area. (Bottom) A regional cross-section outlining the structure and location of our  
754 study area in the Outer Kwanza Basin on the Angolan passive margin.

755 **Figure 2:** D-L data for extensional faults on a log-log plot extracted from global studies (blue):  
756 (Nicol et al., 1996, McLeod et al., 2000, Young et al., 2001, Nicol et al., 2005, Morley, 2007,  
757 Baudon and Cartwright, 2008, Xu et al., 2011, Tvedt et al., 2013, Whipp et al., 2014, Reeve et  
758 al., 2015, Duffy et al., 2015, Tvedt et al., 2016, Ghalayini et al., 2016, Reilly et al., 2016, Khalil  
759 and McClay, 2017, Morley, 2017, Worthington and Walsh, 2017, Torabi et al., 2019). The D-  
760 L fault data presented within this study are also shown (orange). Note that the D-L data sit  
761 within global D-L patterns and, that on this scale, adhere to scaling laws (i.e.  $D = cLn$ ), despite  
762 that the data presented revealing deviations from D-L scaling relationships in their geometry  
763 and growth histories (see text for full discussion).

764 **Figure 3:** A seismic overview of the structure and stratigraphy of the study area, highlighting  
765 the key stratigraphic and structural elements in this study. Data courtesy of CGG Multi-Client.

766 **Figure 4:** (a-d) Depth structure maps of the Intra-Pliocene, Top Miocene, Top Eocene and Top  
767 Albian surface, respectively. The temporal and spatial presence of each of the studied faults is  
768 also highlighted on each of the structure maps. The Top Albian surface is not offset by any of  
769 the faults and shows the location of seismic sections for figure 5.

770 **Figure 5:** (a) Left. (b) Right. Seismic cross-sections of planar (F1-4) and bifurcated (F6-7)  
771 faults showing their dip and interaction with each of the key Intra-Pliocene, Top Miocene and  
772 Top MTC surfaces, shown with depth respectively. Here, the bifurcated faults show bifurcating

773 upward fault segments with narrow relay zones and offset the Top MTC horizon. Data courtesy  
774 of CGG Multi-Client.

775 **Figure 6:** An overview of fault terminology; including the defined terms for calculating aspect  
776 ratio (top) and determining the geometry of a fault (bottom).

777 **Figure 7:** A variance extraction (-1400 m) of meandering channels (right). Seismic sections of  
778 the erosional channels observed in the variance extraction within the shallow stratigraphy of  
779 the area (c. 200-250m below seabed). The erosional bases of these channels erode the upper  
780 tips of faults (e.g. F3). In the case where upper fault tips offset the channel deposits (e.g. F4,  
781 F6 and F7) it is likely any previous growth packages of near-seabed growth have been eroded.  
782 Data courtesy of CGG Multi-Client.

783 **Figure 8:** (a) A variance extraction of the Intra-Pliocene surface and the locations of F1-4. (b-  
784 e) Strike projections for F1-4, respectively. They display the geometry of, and throw  
785 distribution on, the fault surfaces with the Intra-Pliocene and Top Miocene surfaces,  
786 respectively with depth. Unrestricted faults (F1-2; b-c) display throw maxima in Pliocene  
787 stratigraphy which decrease towards their tips. Restricted faults (F3-4; d-e) display throw  
788 maxima positioned towards their lower tips in Miocene stratigraphy. The aspect ratios for F1-  
789 2 (b-c) are 0.01, and are 0.12 and 0.11 for F3-4 (d-e), respectively. The aspect ratios for F1-2  
790 is 2.7, while F3 and F4 have greater aspect ratios of 3.7 and 5.2, respectively.

791 **Figure 9:** Fault height - length data for all fault groups within the studied array. Overall, a trend  
792 is observed of fault height increasing proportionally with fault length. However, faults which  
793 tip out down dip at the Top MTC surface and have high aspect ratios (F3-4) show increasing  
794 fault length without a proportional increase in fault height (red), as predicted for vertically  
795 restricted faults (Fig. 12).

796 **Figure 10:** A seismic section of the position of unrestricted faults (F1-2) within the  
797 stratigraphy. Their lower tips do not interact with the MTC layer. A t-z plot for F1 where the  
798 EI on the upper tip is *c.* 1.2 (left). T-z plots (F1-4) showing that restricted faults exhibit throw  
799 maxima in Miocene stratigraphy and unrestricted faults exhibit throw maxima in Pliocene  
800 stratigraphy (right). Data courtesy of CGG Multi-Client.

801 **Figure 11:** (a) A seismic cross-section showing the tips of F3-4 tipping out downdip on top of  
802 the MTC surface and the adjacent bifurcating faults (F6-7) offsetting the Top MTC surface.  
803 Above, the maximum throw of the respective faults are displayed and the proposed  
804 accumulated strain needed to overcome the threshold for onward growth through the MTC  
805 (grey box). (b) Throw-length data for the fault array displaying that faults with maximum  
806 throws  $> 30$  m offset the MTC, while faults with throw values  $< 30$  m which interact with the  
807 MTC are vertically restricted. T-x regression analysis for the array's data also suggests the  
808 constant length model for fault growth [i.e.  $T > 0$  where  $L = 0$ ]. (c) T-x plots for faults restricted  
809 by the MTC (F2-3) and some which achieve onward propagation (F6-7, A4). Data courtesy of  
810 CGG Multi-Client.

811 **Figure 12:** A sketch diagram portraying the effects of vertical restriction by a mechanical layer  
812 (MTC) during fault growth and its predicted effect on fault geometrical data as a result of  
813 growth with preferential lengthening. Adapted from Soliva et al. (2005b).

814 **Figure 13:** Strike projections for the bifurcating faults (F6 and F7), displaying the geometry  
815 of, and throw distribution on, the fault surfaces with the Intra-Pliocene, Top Miocene, Top  
816 MTC and Top Eocene surfaces, respectively with depth. (a) F6: Maximum throw lies beneath  
817 the Top MTC surface and relay branchline (blue area). Overall, greater throw values encircle  
818 the relay zone which is associated with a throw minimum (white area). High throw gradients  
819 (*c.* 0.2) are present at the transition from the fault surface to the relay zone (sharp transition

820 from blue to white area). (b) F7: Maximum throw lies coincident with the Top MTC surface  
821 on the main fault surface. Overall, greater throw values are present along strike at the structural  
822 level of the Top MTC surface.

823 **Figure 14:** Sketch diagrams of proposed growth histories for bifurcating faults. (a) F7:  
824 Individual precursor fault segments become vertically restricted by the regionally extensive  
825 MTC during downward propagation. As a result of this restriction precursor faults  
826 preferentially lengthen via segment linkage and the throw maxima migrate downwards as strain  
827 accumulation occurs at the restricted tip. Eventual strain accumulation overcomes the MTC  
828 restricting influence and continues downward propagation. (b) F6: Similarly to F7, an initial  
829 vertical restriction results in strain accumulation and throw maxima migration towards the  
830 MTC. Following overcoming the MTC's restricting influence, bifurcation at the MTC  
831 boundary occurs.

832 **Figure 15:** (a) A plot showing the relationship between the maximum throw on arcuate faults  
833 and their distance from the salt wall. In this fault group, the maximum throw observed on faults  
834 increases as the faults become more proximal to the salt wall. The deeper arcuate subgroup  
835 (A1-4) exhibit greater throws than the shallower (A5-9) subgroup. (b) A comparative plot of  
836 throw - length data between arcuate faults and that of other groups which exhibit similar  
837 maximum throw values. This plot highlights that, in comparison to other fault groups, arcuate  
838 faults are overdisplaced.

839 **Figure 16:** A variance co-blended depth structure map of the Intra-Pliocene surface (top right)  
840 showing the location of the seismic section showing the present-day structure of the salt  
841 minibasin (bottom right). The structure map also highlights the deeper part of the minibasin in  
842 the south and the onlap surface onto the salt wall. Hatched = presence of salt wall at this  
843 structural level. (a-d) A sketch diagram of the evolution of the minibasin in relation to the

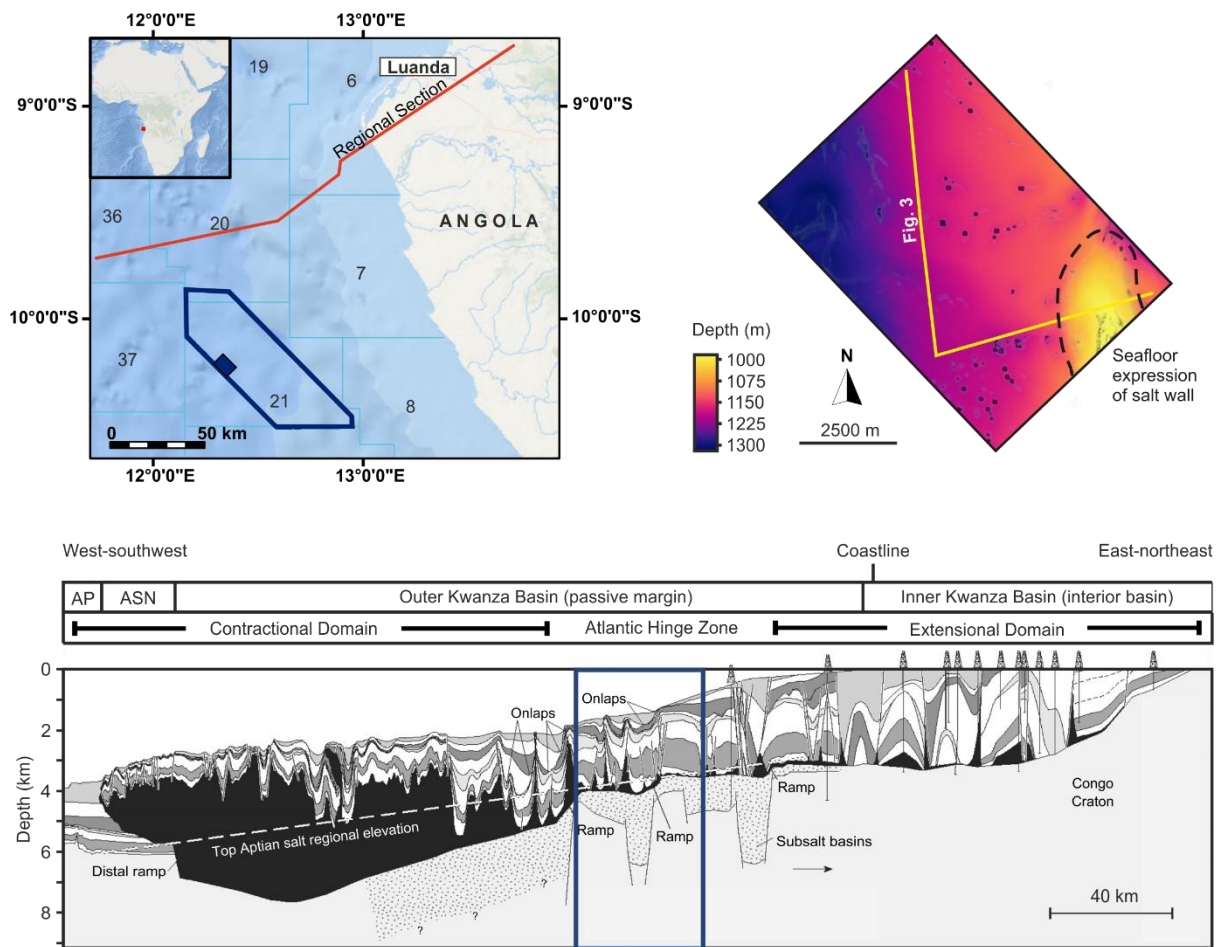
844 arcuate fault group. Evolution includes: a) sediment loading, b) salt withdrawal, diapirism, c-  
845 d) outer-arc bending and the subsequent onset of the nucleation of extensional arcuate faults.

846 Data courtesy of CGG Multi-Client.

847

848

849 **Figure 1**



850

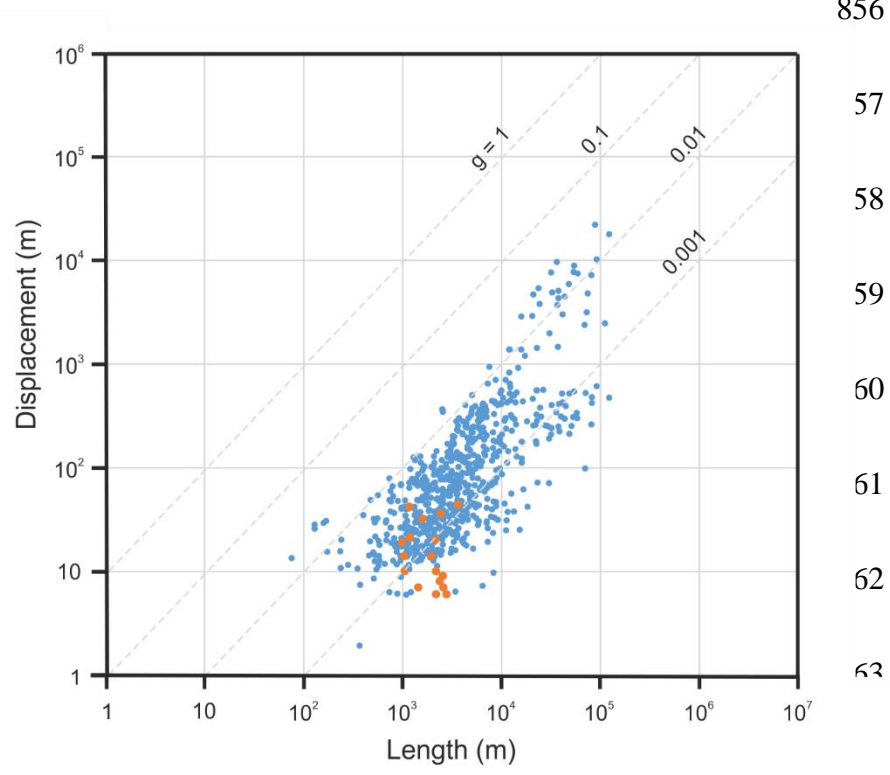
851

852

853

854

855 **Figure 2**



856

57

58

59

60

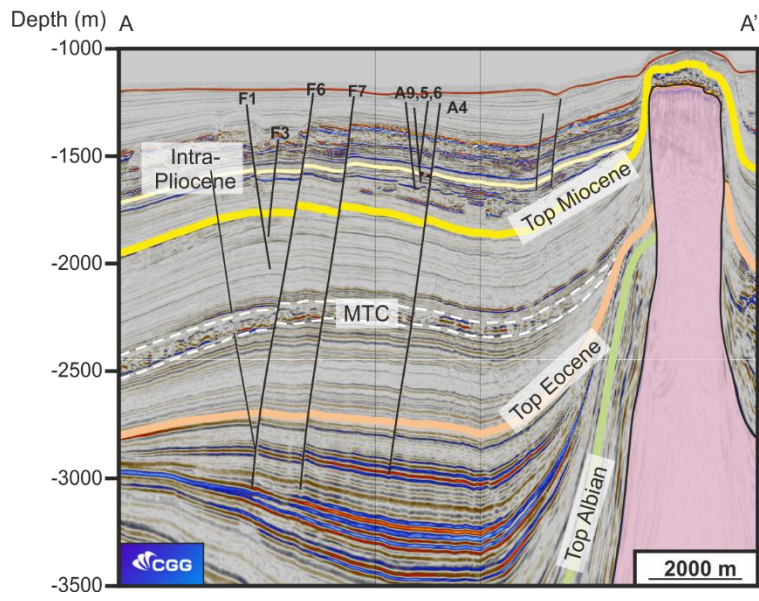
61

62

63

865

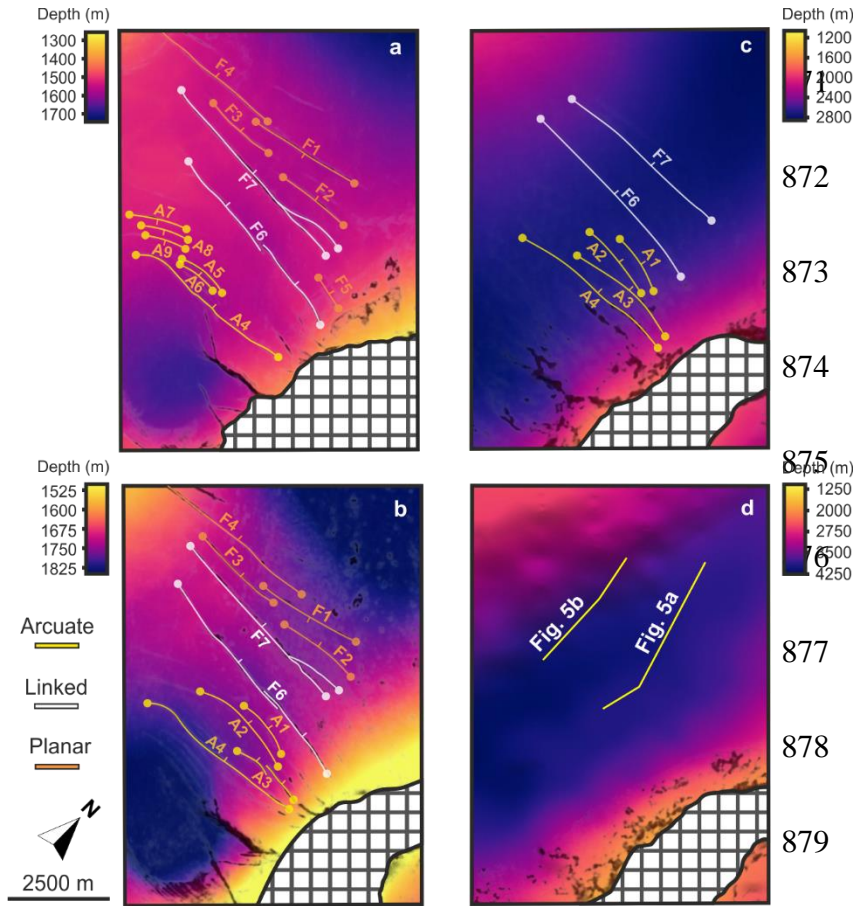
866 **Figure 3**



868

869 **Figure 4**

870



872

873

874

875

877

878

879

880

881

882

883

884

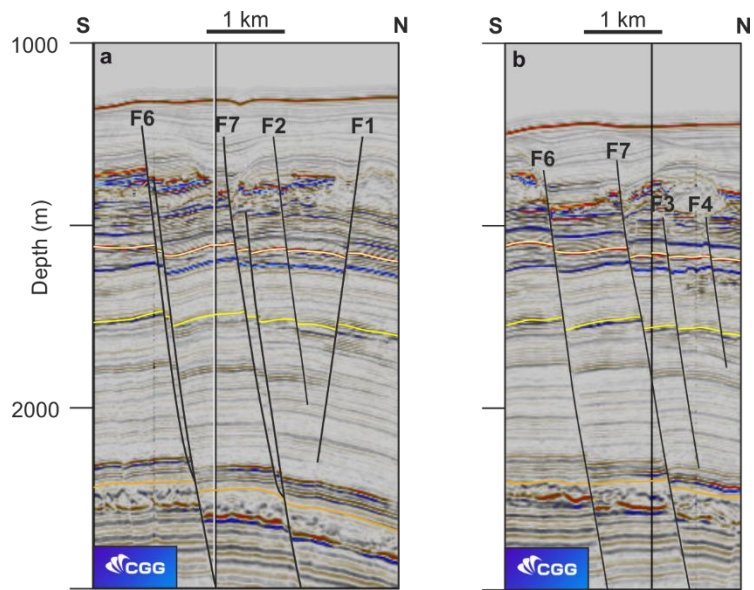
885

886

887

888

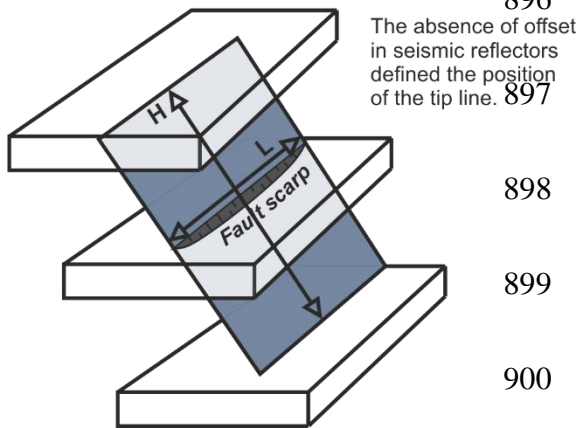
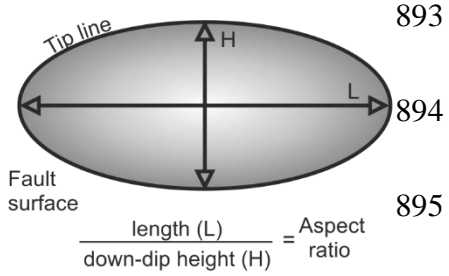
889 **Figure 5**



890

891

892 **Figure 6**



901

902

903

904

905

906

907

908

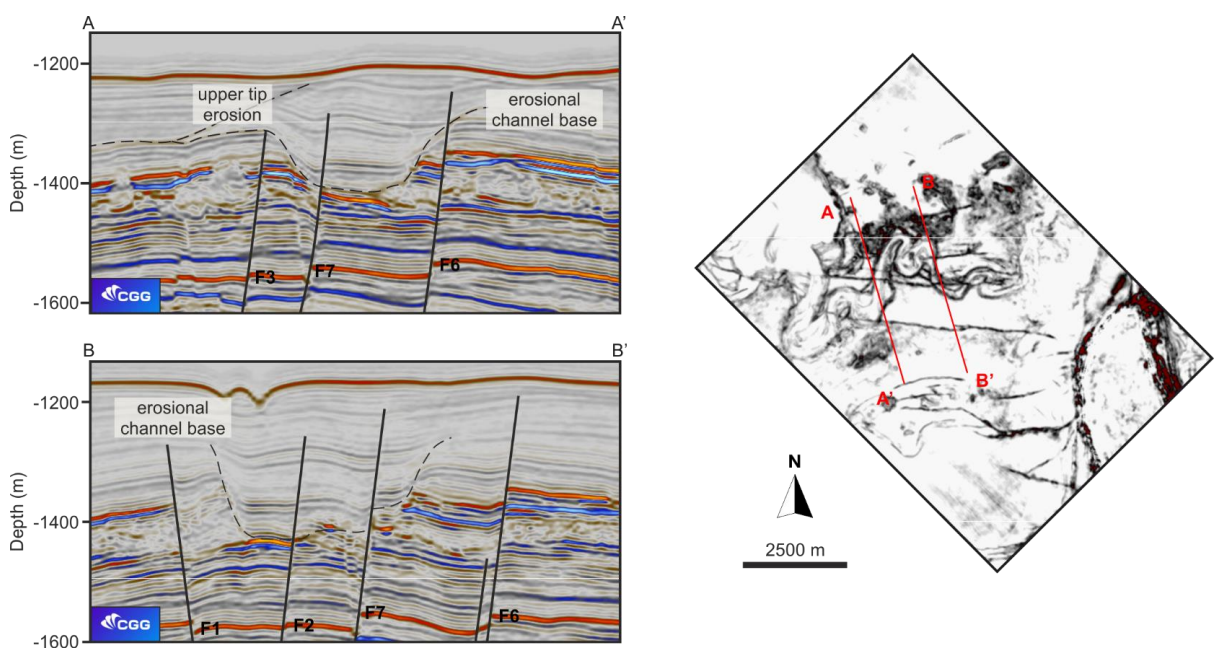
909

910

911

912 **Figure 7**

913

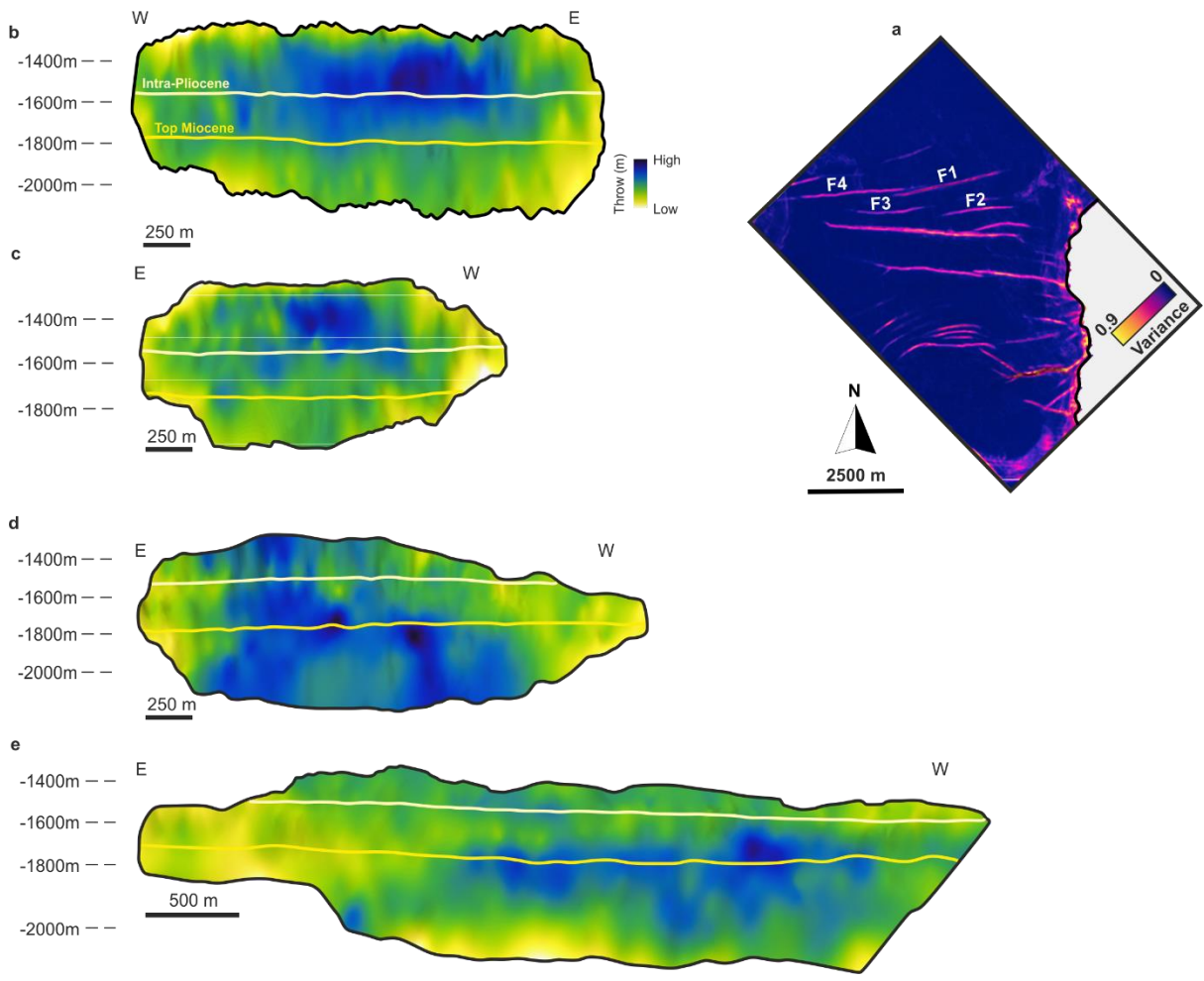


914

915

916

917 **Figure 8**



918

919

920

921

922

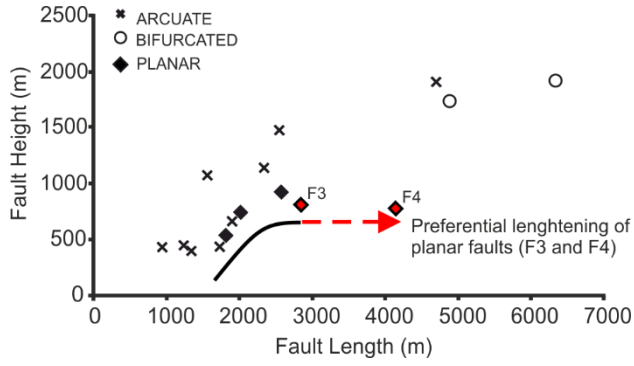
923

924

925

926 **Figure 9**

927

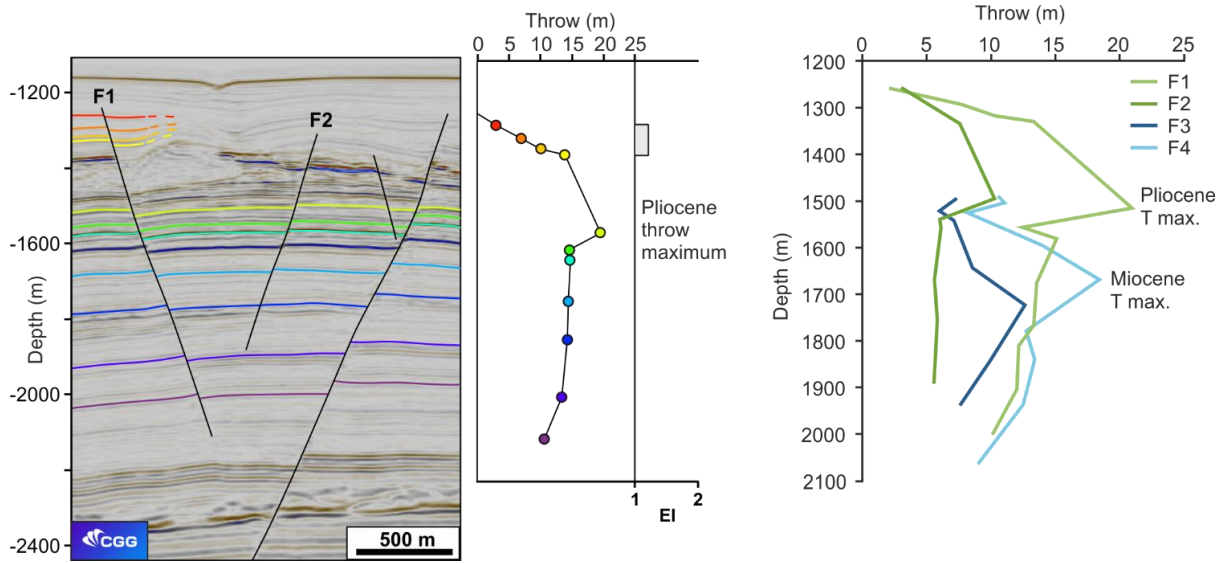


928

929

930

931 **Figure 10**



932

933

934

935

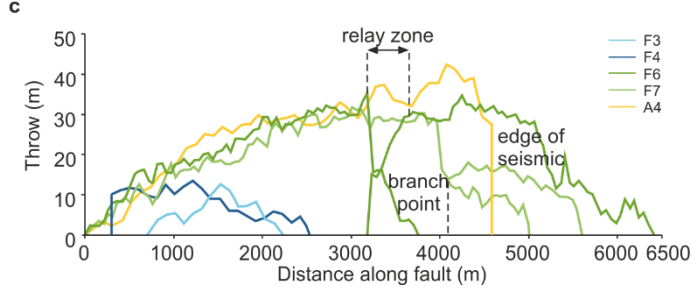
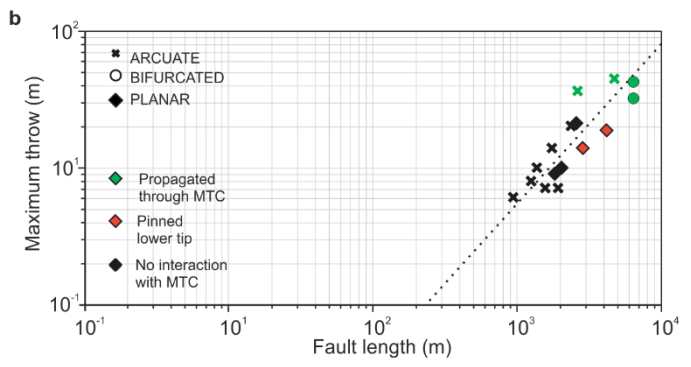
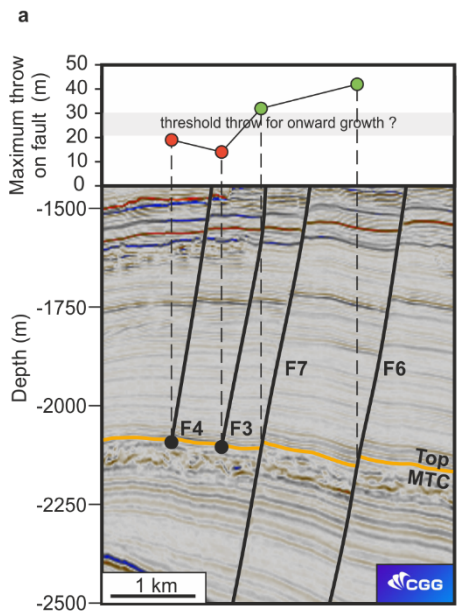
936

937

938

939 **Figure 11**

940

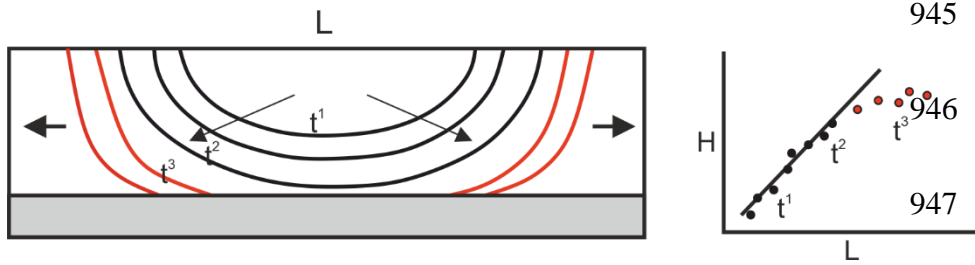


941

942

943

944 **Figure 12**



948

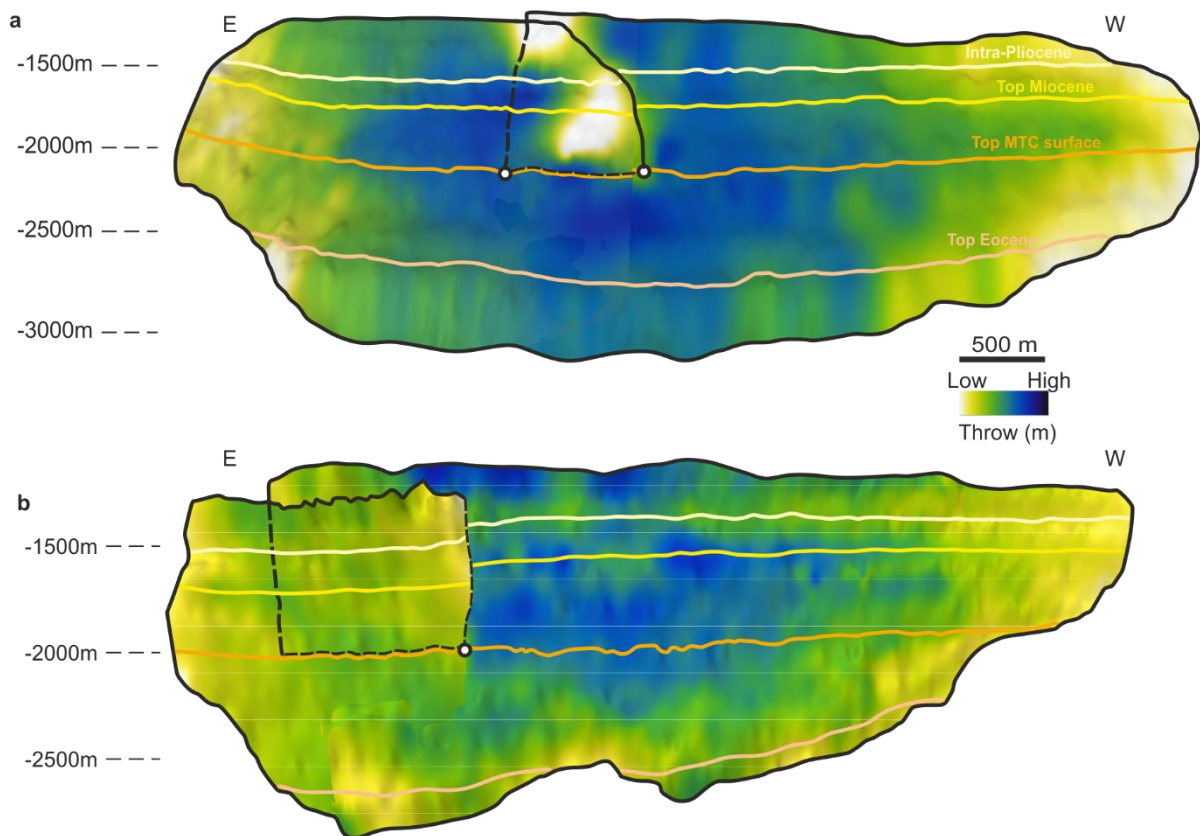
949

950

951

952 **Figure 13**

953

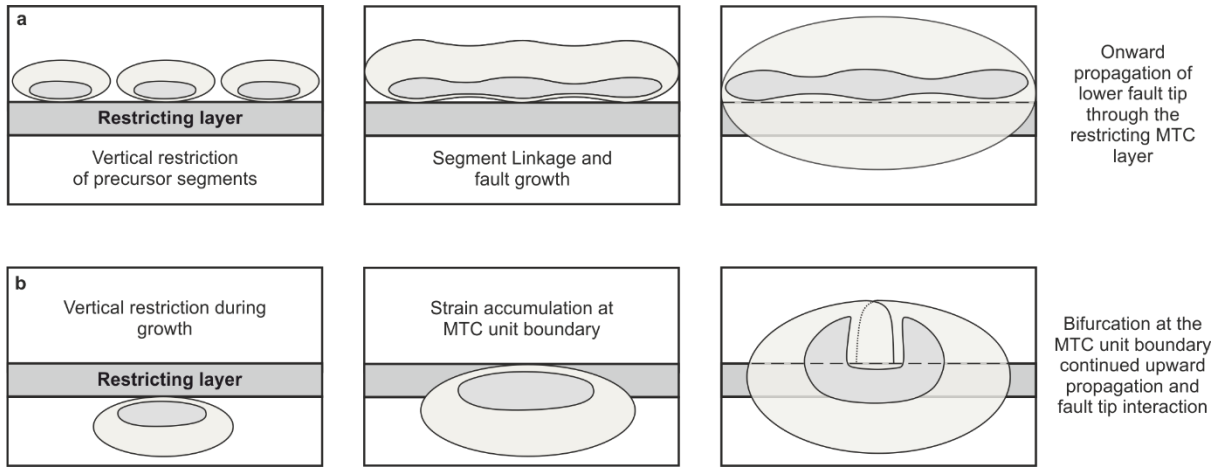


954

955

956

957 **Figure 14**



958

959

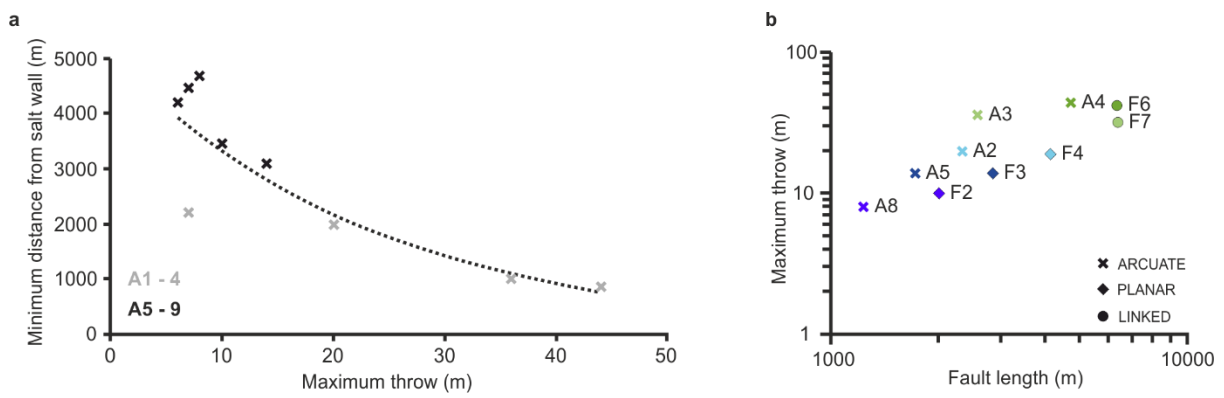
960

961

962

963 **Figure 15**

964

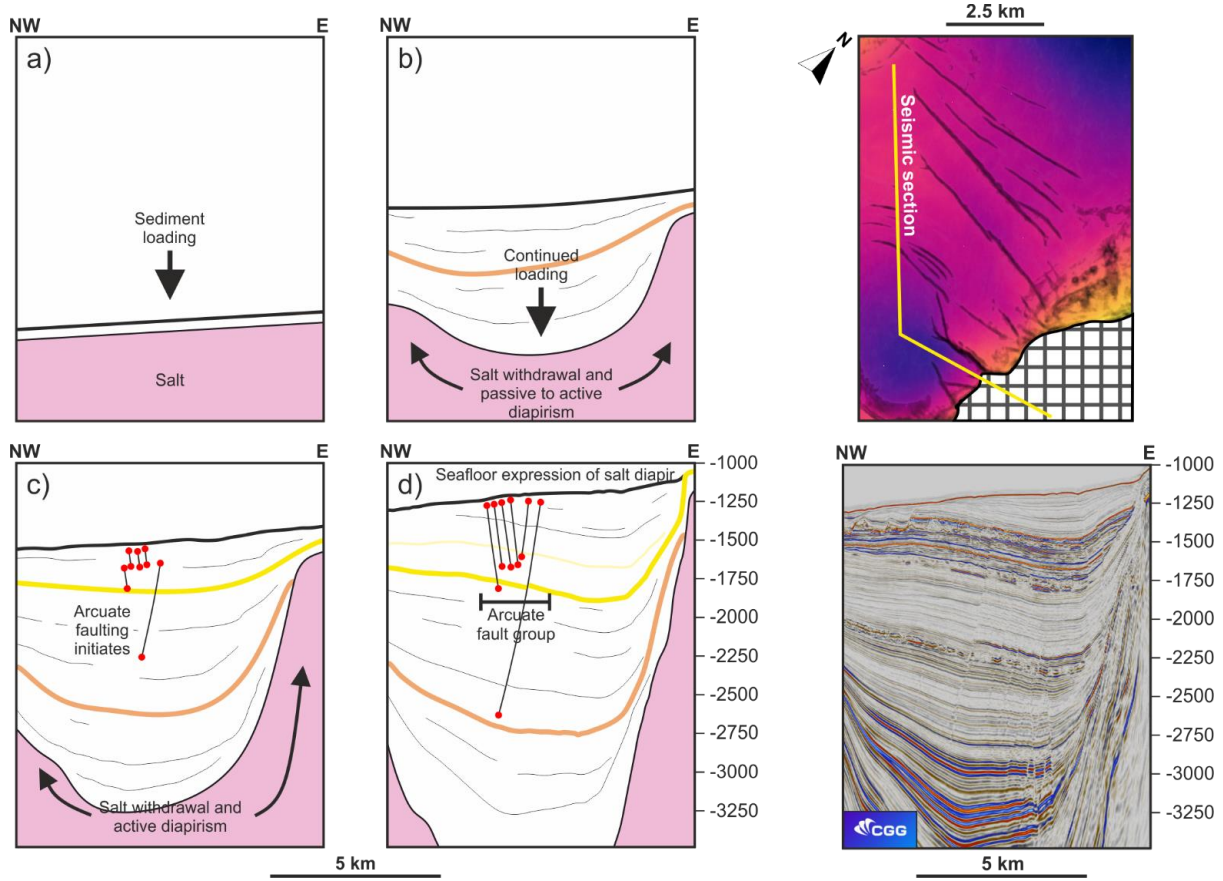


965

966

967

968 **Figure 16**



969

970

971

972